Experimental Reports

(2018)

Activity Report on Neutron Scattering Research: Experimental Reports Vol. 24 (2018)

Published by:
Neutron Science Laboratory,
Institute for Solid State Physics,
University of Tokyo
106-1, Shirakata, Tokai,
Ibaraki 319-1106,
JAPAN

This volume contains experimental reports submitted in the following period of time: 2018/8/1 to 2019/7/31.
Visit our on-line database for updated information.

Structures and Excitations

Magnetism

- Determination of the Magnetic Structure under Magnetic Field of the Noncentrosymmetric Heavy-Electron Metamagnet CePtSi3
  Daichi Ueta, Yoichi Ikeda, Takatsugu Masuda, and H. Yoshizawa
  Activity Report on Neutron Scattering Research: Experimental Reports **24** (2018) Report Number: 1919

- Spin excitations in the magnetic skyrmion-lattice phase
  Seno Aji, Shinichiro Yano, and Taku J Sato
  Activity Report on Neutron Scattering Research: Experimental Reports **24** (2018) Report Number: 1922

- Neutron diffraction study on the Pd-Ga-Tb 2/1 quasicrystal approximant
  Taku J. Sato, Maxim Avdeev, Kyohei Takagi, and Yeong-Ge So
  Activity Report on Neutron Scattering Research: Experimental Reports **24** (2018) Report Number: 1923

- Neutron diffraction study on the Yb3Ru4Al12 itinerant kagome antiferromagnet
  Taku J Sato, Noriyuki Kabeya, Maxim Avdeev, Shintaro Nakamura, and Akira Ochiai
  Activity Report on Neutron Scattering Research: Experimental Reports **24** (2018) Report Number: 1924

- Dynamics of the magnetic skyrmion under an alternative current in MnSi
  D. Okuyama, M. Bleuel, Q. Ye, A. Kikkawa, Y. Taguchi, Y. Tokura D. Higashi, J. D. Reim, Y. Nambu, and T. J. Sato
  Activity Report on Neutron Scattering Research: Experimental Reports **24** (2018) Report Number: 1925

- Determination of the spin system in Ni2V2O7 using neutron diffraction in magnetic fields
  Masashi Hase Matsuo, James R. Hester, and Kirrily C. Rule
  Activity Report on Neutron Scattering Research: Experimental Reports **24** (2018) Report Number: 1931

- Full control of magnetic moment in multiferroics Ba2CoGe2O7
  Shunsuke Hasegawa and Takatsugu Masuda
  Activity Report on Neutron Scattering Research: Experimental Reports **24** (2018) Report Number: 1933

- Quantum spin liquid state of Tb2+xTi2-xO7+y
  H. Kadowaki, B. F{aa}k, J. Ollivier, T. J. Sato
  Activity Report on Neutron Scattering Research: Experimental Reports **24** (2018) Report Number: 1935

Strongly Correlated Electron Systems

- Investigation of vortex lattices on non-centrosymmetric superconductor LaNiC2
  M. Soda, V. Ryukhtin, P. Strunz, and H. Furukawa
  Activity Report on Neutron Scattering Research: Experimental Reports **24** (2018) Report Number: 1901

- Investigation of magnetic ordering in high pressure phase of DyMnO3
  Noriki Terada, Navid Qureshi, Mechthild Enderle, Fabio Orlandi, Dmitry Khalyavin, Pascal

Manuel and Dharmalingam Prabhakaran
Activity Report on Neutron Scattering Research: Experimental Reports **24** (2018) Report Number: 1906

- Nesting features and the superconducting mechanism in Ce(Co,Rh)In5
  Kanae Shinohara
  Activity Report on Neutron Scattering Research: Experimental Reports **24** (2018) Report Number: 1914

Biology

- Elucidation of tri-ubiquitin dynamics concerning about status of interaction interfaces
  Masaaki Sugiyama, Rintaro Inoue, Ken Morishima, Maho Yagi-Utsumi, Methanee Hiranyakorn, Michihiro Nagao, Hiroshi Nakagawa
  Activity Report on Neutron Scattering Research: Experimental Reports **24** (2018) Report Number: 1926

Soft Matters

- Solvent dependence in Platonic structures of resorcinarene-based capsule
  Shota Fujii, Kazuo Sakurai
  Activity Report on Neutron Scattering Research: Experimental Reports **24** (2018) Report Number: 1900

- Elucidating hydration state of poly (propylene oxide) in the glyco polymer vesicle membranes by SANS measurement.
  Tomoki Nishimura
  Activity Report on Neutron Scattering Research: Experimental Reports **24** (2018) Report Number: 1904

- Distribution of Additives in Ordered-Bicontinuos-Double-Network Structure Formed in Block Copolymer Systems Revealed by Small Angle Neutron Scattering
  Katsuhiro Yamamoto, Tsukasa Miyazaki, Isamu Akiba
  Activity Report on Neutron Scattering Research: Experimental Reports **24** (2018) Report Number: 1908

- Investigation of Microscopic Structural Changes in Poly(oligo-ethylene glycol methyl ether methacrylate)-Based Hydrogels
  Takuma Kureha, Xiang Li
  Activity Report on Neutron Scattering Research: Experimental Reports **24** (2018) Report Number: 1911

- Structural Characterization of DNA-module gel by Small-Angle Neutron Scattering
  Masashi Ohira, Xiang Li, and Mitsuhiro Shibayama
  Activity Report on Neutron Scattering Research: Experimental Reports **24** (2018) Report Number: 1920

- Length dependent effect of added alkane on fluidity and inter-leaflet coupling of lipid membranes
  Hatsuho Usuda, Mafumi Hishida, Elizabeth Kelley, Michihiro Nagao
  Activity Report on Neutron Scattering Research: Experimental Reports **24** (2018) Report Number: 1928

- Investigation of Microscopic Structural Changes in Poly(oligo-ethylene glycol methyl ether methacrylate)-Based Hydrogels
  Takuma Kureha, Xiang Li
  Activity Report on Neutron Scattering Research: Experimental Reports **24** (2018) Report Number: 1932

Structures and Excitations

Phonon dynamics on thermoelectric material of Mg3Sb2

C. H. Lee1, H. Kunioka1, H. Mori2, T. Hasegawa3
1AIST, Japan, 2Osaka Univ., Japan, 3Hiroshima Univ., Japan

Thermoelectric power generation is expected to contribute to energy conservation through the generation of electricity from waste heat. To realize this technique, intense efforts have been devoted to improving the performance. The difficulty in improving material performance comes from the conflicting requirements to exhibit high electrical conductivity while keeping the thermal conductivity low.

Mg3Sb2 is one of promising candidate exhibiting high thermoelectric performance. It shows high value of the dimensionless figure of merit ZT ~ 1.65 with quite low lattice thermal conductivity of kL ~ 0.7 W/mK at T = 725 K [1,2]. Great attention has been attracted in this compound for the origin of its low kL. One assumption is based on the existence of lone pairs around Sb atoms. It has been argued that interatomic potential could be anharmonic due to lone pairs, thus, heat carrying phonons can be heavily scattered. But there is no clear evidence about the claim. Therefore, phonon must be studied using inelastic neutron scattering.

In this experiment, we aim to clarify the origin of low kL of Mg3Sb2 by examining phonons at FRM2 using PUMA. The weight of Mg3Sb2 single crystal was 1.21 g. Measurements were done on scattering planes of (hk0) and (hhl) to cover wide range of Brillouin zone. Phonon calculations were performed using the ABINIT program.

Mg3Sb2 has CaAl2Si2-type crystal structure with the P-3m1 space group. Mg atoms occupy both Ca and Al sites. Thus, it is basically a 122 Zintl phase compound. Charge density calculations on SrZn2Sb2 that has the same crystal structure as Mg3Sb2 reveal the existence of lone pairs around Sb atoms [3].

Figure 1 shows phonon dispersion at T = 298 K. Solid lines are results of calculations. Overall, observed peaks agree well with the calculations, ensuring the correctness of the mode assignment. Observed modes are demonstrating by colored lines. Gray lines are remaining modes that we must measure next time. To find anharmonic phonons that can be the origin of low lattice thermal conductivity in Mg3Sb2, we will measure temperature dependences in the near future. Further experiments are required to obtain overall picture of phonon dynamics and to clarify the role of lone pairs that are believed to be responsible for the anharmonicity.

[1] H. Tamaki et al., Adv. Mater. 28, 10182 (2016). [2] J. Zhang et al., Nature Commun. 8, 13901 (2017). [3] E. S. Toberer et al., Dalton Trans. 39, 1046 (2010)

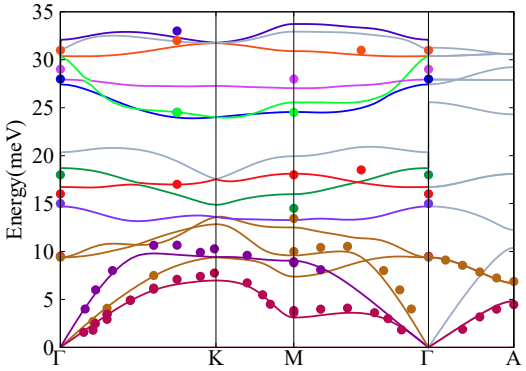

Fig. 1. Phonon dispersions of Mg3Sb2 at T = 298K. Solid lines are results of calculations. Color and gray lines depict observed and unobserved modes, respectively.

Structure and catalytic activity of PdRu alloy nanoparticles

O. Yamamuro[A], H. Akiba[A], K. Kusada[B], M. Haneda[C], H. Kitagawa[B], D. Keen[D]
[A]*ISSP-NSL, Univ. of Tokyo,* [B]*Kyoto Univ.,* [C]*Nagoya Institute of Technology,* [D]*ISIS, RAL*

Recently, metal nanoparticles attract much attention as catalytic systems for chemical reactions of gasses. We focus our attention on PdRu-based alloys since they are expected to be high-performance and low-cost catalysts to remove CO and NOx in exhaust gas of cars. Pd and Ru form bulk solid solutions only at much higher temperatures than room temperature. This is mainly because Pd has an fcc structure while Ru has an hcp one. We have found that Pd_xRu_{1-x} with a diameter of 5-7 nm are miscible in the whole composition range around room temperature [1]. However, there is still microscopic phase separation between the fcc and hcp phases in a single nanoparticle and transpiration of Ru atoms occurs at higher temperatures. It is the present largest problem why the endurance of catalytic ability strongly depends on the composition of the flow gases which are similar to actual exhaust gases of cars:

Stoichi: NO:0.15%, O_2:0.3%, CO:0.35%, C_3H_6:0.033%, H_2:0.1%

Rich: NO:0.15%, O_2:0.15%, CO:0.35%, C_3H_6:0.033%, H_2:0.1%

Lean: NO:0.15%, O_2:0.45%, CO:0.35%, C_3H_6:0.033%, H_2:0.1%

Rich and lean correspond to amounts of CO gas compared with the stoichiometric compositions for the CO and C_3H_6 oxidization and NO reduction; we change the ratio of O_2 gas in the actual experiments as shown above. In this study, we have performed the neutron powder diffraction (NPD) experiments on PdRu nanoparticles supported on CZ (CeO_2-ZrO_2) to elucidate the structural change of nanoparticles caused by the catalytic reactions with the three gases given above. The NPD measurements were performed using the high-intensity neutron powder diffractometer (GEM) installed at RAL, ISIS. NPD is powerful to distinguish between neighboring atoms in the periodic table such as Pd and Ru.

Figure 1 shows the NPD patterns of $Pd_{0.5}Ru_{0.5}$ nanoparticles supported on CZ before and after the Rich and Lean gas treatments at 673 K. The black, blue and red bars represent the peak positions calculated for the fcc structure of CZ, and the fcc and hcp structures of PdRu nanoparticles, respectively. The Lean sample (blue curve) has larger fcc intensity than the Rich sample (red curve). This result indicates that Ru atoms inside the nanoparticles move to the surface and the Pd-rich fcc phase increases in the interior region. This is consistent with our previous IR study and will be more definite by an on-going pdf (pair-distribution function) analyses. It should be noted that this is the first in-situ NPD data showing the structural change of nanoparticles due to catalytic reactions.

[1] K. Kusada et al., J. Am. Chem. Soc. 136, 1864 (2014).

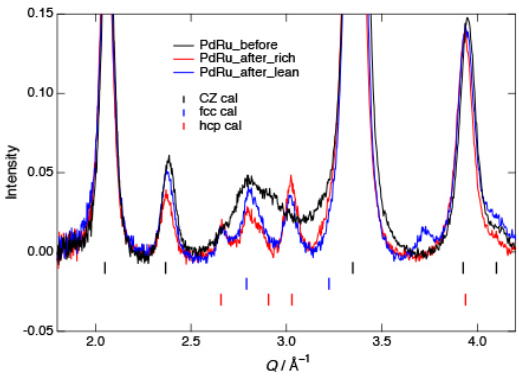

Fig. 1. Neutron diffraction patterns of $Pd_{0.5}Ru_{0.5}$ nanoparticles supported on CZ before (black) and after (red and blue) the catalytic reactions with Rich and Lean gases.

Crystal structure analysis of high temperature neutron diffraction data of novel oxide-ion conductor HoGaTi2O7

Kotaro Fujii, Yuta Yasui, Masatomo Yashima
Tokyo Institute of Technology

Oxide-ion conductors, which include pure ionic conductors and mixed oxide-ion and electronic conductors, attract significant interest because of their varied uses in oxygen separation membranes and cathodes for solid-oxide fuel cells (SOFCs). The oxide-ion conductivity is strongly dependent on the crystal structure. At present, several structures, such as fluorites, perovskites, K_2NiF_4, mellilites, and apatites, are known to show high oxide-ion conductivities. For further development of oxide-ion conductors is investigating materials with new types of structures. According to such background, we are exploring new structure family of oxide-ion conductors. For example, we have discovered a new structural family of oxide-ion conductor $BaNdInO_4$ which has a monoclinic $P2_1/c$ perovskite-related phase with a layered structure, in 2014. More recently, we found novel material, $SrYbInO_4$ with $CaFe_2O_4$-type structure, showed higher oxide-ion conductivity compared to the other $CaFe_2O_4$-type materials. In order to understand the mechanism of oxide-ion conduction, it is necessary to precisely determine the crystal structure (particularly position, occupancy factor, and anisotropic displacement parameters of oxygens) at high-temperature because oxide-ion conductors are generally used at high-temperature. In the present study, we investigated the crystal structure of $HoGaTi_2O_7$ at high temperature using high resolution neutron powder diffractometer Echidna installed at the research reactor OPAL, ACNS, ANSTO. The material was prepared by the solid-state reaction. Sintered pellets of the reaction products were introduced into a vanadium can and used for the neutron diffraction experiment. The measurements were carried out from room temperature to high temperature (1000 °C). Each measurement took about 6 hours. The structural analyses for these data are carried out by Rietveld method using the program RIETAN-FP. The Rietveld structure refinements of the diffraction data of $HoGaTi_2O_7$ taken at the room temperature 23 °C, and 1000 °C using the orthorhombic *Pbcn* $GdGaTi_2O_7$-type structure gave good quality of the fit and the reliability factors (R_{wp} =2.31 %, R_B = 1.48 % for 23 °C data, and R_{wp} = 2.07 %, R_B = 2.44 % for 1000 °C data). The unit-cell parameters and unit-cell volume V of $HoGaTi_2O_7$ at 1000 °C (a = 9.8658(3) Å, b = 7.4117(2) Å, c = 13.6497(4) Å, V = 998.09(5) Å^3) are larger than those at RT (a = 9.77095(16) Å, b = 7.35349(13) Å, c = 13.5334(2) Å, V = 972.38(3) Å^3), due to the thermal expansion. The bond lengths and equivalent isotropic atomic displacement parameters of $HoGaTi_2O_7$ at 1000 °C are higher than those at RT, which indicates the larger thermal vibration at 1000 °C. The higher equivalent atomic displacement of oxygen atoms at 1000 °C suggests higher oxide-ion conductivity at 1000 °C compared to RT.

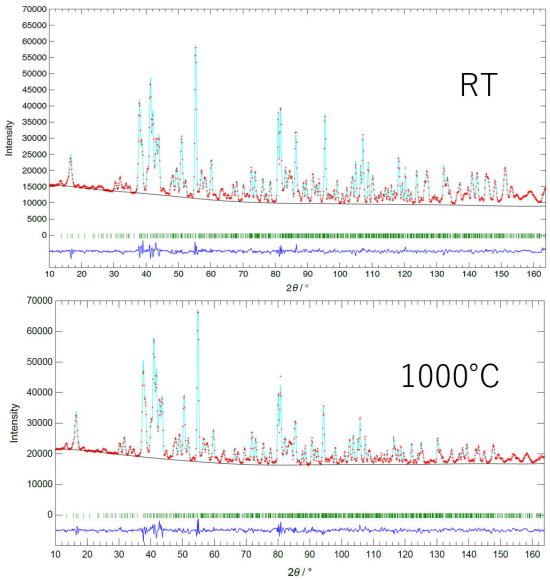

Fig. 1. Results of Rietveld refinement

Magnetism

Magnetic structure of Spin S=1/2 linear trimer system Na2Cu3Ge4O12

Yukio Yasui (A), Rusei Toma (A), Lukas Keller (B), and Jonathan White (B)
(A) Meiji University, (B) Paul Scherrer Institut

Low dimensional quantum spin systems attract much attention. In particularly, the frustrated quantum spin systems due to geometrical arrangement or competing interactions are expected to exhibit various interesting properties. Na2Cu3Ge4O12 has a Cu3O8 trimer formed of edge-sharing three CuO4 square planes [1]. For Cu2+ spins (S=1/2) within the Cu3O8 trimer, the second-neighbor exchange interaction J2 is antiferromagnetic (J2 >0) ,and the nearest-neighbor exchange interaction J1 is weak ferromagnetic or antiferromagnetic (AF). Such competing interactions between J1 and J2 can lead to novel quantum magnetic phenomena.

The T-dependence of magnetic susceptibility χ of Na2Cu3Ge4O12 in the T-region 70 K $<$ T $<$ 650 K can be explained by the isolated S = 1/2 Heisenberg trimer model, and it is obtained J2/kB = 340 $\pm$ 20 K (AF), and J1/kB = 30 $\pm$ 20K. [2] On the other hand, T-dependence of χ of Na2Cu3Ge4O12 in the T-region 4 K $<$ T $<$ 70 K can be explained by the S = 1/2 uniform Heisenberg chain model called as Bonner-Fisher model [3], and it is obtained J3/kB = 18 $\pm$ 1 K where J3 is an inter-trimer exchange interaction.[2] The ground state of the isolated S = 1/2 trimer is found that two spins of the edge in the Cu3O8 trimers form a nonmagnetic singlet state by strong AF interaction J2. The center spin of the Cu3O8 trimer only survives in low T-region T $<$ 70K. The behavior of the specific heat in the T-region 4 K $<$ T $<$ 70 K can also be explained by the S = 1/2 uniform Heisenberg chain model. As results of measurements of magnetic susceptibility, specific heat, and dielectric constant, the center spin of the Cu3O8 trimer of Na2Cu3Ge4O12 exhibits an antiferromagnetic transition at TN = 2 K accompanied with a ferroelectricity (called multiferroic phenomenon). From the detailed magnetization measurements, we found the existence of dM/dH anomaly at Hc = 0.37 T at T = 1.9 K ($<$ TN). It is indicating that the magnetic structure changes at Hc. The determination of the magnetic structure at H = 0 and H = 1T ($>$ Hc) give us important information to understand the magnetic behavior of the S = 1/2 linear trimer system.

We investigated the magnetic structure of Na2Cu3Ge4O12 below TN through powder neutron diffraction experiments using cold neutron powder diffractometer DMC at PSI. We used amount of 15 g of powder for Na2Cu3Ge4O12. The superconducting magnet and the dilution refrigerator waer used to reach down to 0.1 K and up to 1 T.

We obtained powder neutron diffraction patterns at T = 0.1 K, 3K, and 12 K, respectively, in H = 0 as well as that of T = 0.1 K applied the magnetic field H = 1T. The figure (a) show the diffraction patterns at T=0.1 K and 12 K, respectively. We can clearly observe the super-lattice magnetic Bragg peaks below TN assigned by the arrows. The figure (b) show the intensity profile of difference between at T = 0.1 K and 12 K, I (0.1K) ? I (12K). We also found the possible magnetic Bragg peaks assigned by the short arrows. By applied the magnetic field H = 1T, no difference found the magnetic Bragg intensities at T = 0.1 K in the error bar. Then, changing the magnetic structure at Hc seems to be small. Recently, the aligned powder of Na2Cu3Ge4O12 can be obtained in the magnetic field H = 9T. For determination of the magnetic structure of Na2Cu3Ge4O12, the results of the various measurements of the aligned powder give us important information. We are analyzing the neutron diffraction data and various measurements data.

[1] X. Mo et al.: Inorg. Chem. 45 3478 (2006).
[2] Y. Yasui et al.: J. Appl. Phys. 115 17E125

(2014).
[3] J. C. Bonner et al.: Phys. Rev. 135 A640 (1964).

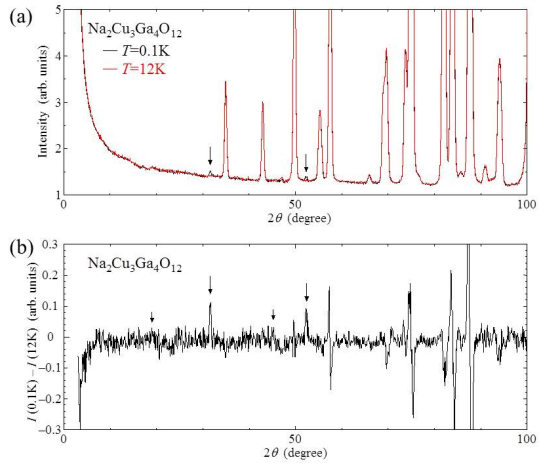

Fig. 1. (a). Neutron powder diffraction patterns measured at 0.1 K and 12 K. The arrows indicate the magnetic Bragg peaks. (b). Intensity profile of difference between at T = 0.1 K and 12 K.

Low Energy Excitations of Magnetic Skyrmions in MnSi

M. Soda and H. Furukawa
RIKEN, Ochanomizu University,

Topological spin textures have been extensively investigated both experimentally and theoretically. Among them, a vortex-like spinswirling texture of so-called magnetic skyrmions has attracted much attention. A helimagnet MnSi possesses a magnetic skyrmion phase in a small magnetic field and temperature region.[1] Since the magnetic skyrmions in MnSi have a long periodicity (˜18 nm), the structure has been examined by using small angle neutron scattering (SANS) and Lorentz Transmission Electron Microscope (LTEM) techniques. On the other hand, the dynamics of magnetic skyrmions has not been clear because inelastic neutron scattering measurements with an energy scale of 1˜5 micro-eV in a small q region is not easy. Then magnetic excitations only in the helical phase has been reported.

Recently, a theoretical study on the magnetic skyrmions has been carried out by our theoretical group[2]. The string of skyrmions appears to be parallel to the magnetic field. Not only the difference between the magnetic dispersions for the helical and skyrmion structures but also the different q dependence of magnetic excitations along +qz and -qz have been predicted.

We have carried out the neutron spin-echo experiment with IN15 installed in ILL in MnSi to clarify the low energy excitation of skyrmion. Figure 1 shows the experimental setting in IN15. The profiles obtained by spin-echo experiment had the large phase shift which corresponds to the energy transfer. This behavior becomes opposite with changing the magnetic field direction. The obtained results mean that the skyrmion has the asymmetric dispersion.

reference
[1] S. Muhlbauer et al., Science 323 (2009) 915.
[2] W. Koshibae et al. private commun.

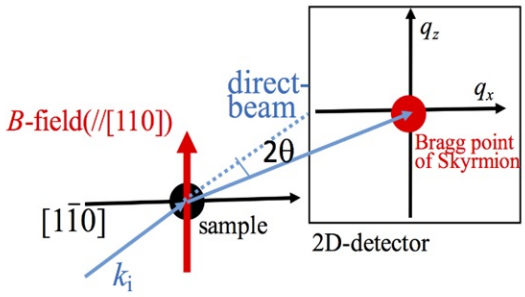

Fig. 1. Experimental setting in neutron spin-echo measurement

Uniaxial-stress-control of domain growth kinetics in isosceles-triangular lattice Ising magnet CoNb2O6

Setsuo Mitsuda, Yutaro Shimoda
Department of Physics, Faculty of Science, Tokyo University of Science

The isosceles triangular lattice (ITL) Ising antiferromagnet is characterized by the ratio of exchange interactions defined as γ = J_1 (along the base direction) /J_2 (along the equilateral direction), and its magnetic property dramatically changes, depending on whether γ is larger than 1.0 or not. As one of the model materials, we have studied an Ising magnet $CoNb_2O_6$, where the quasi-1D ferromagnetic zigzag chains along the *c* axis form a frustrated antiferromagnetic ITL with $\gamma \simeq 1.33$ in the *a*-*b* plane. If the exchange ratio γ can be controlled in $CoNb_2O_6$ via anisotropic deformation of ITL by uniaxial pressure, variety of interesting magnetic features intrinsic to γ would be observed.

Actually along this context, we succeeded in crossing the Wannier point (γ = 1) and providing access to the region of γ < 1 by applying uniaxial pressure p up to 1.1GPa along the *c* axis, where entirely different $H_{\|c}$-T magnetic phase diagram with ground-state AF-I magnetic ordering appears, as is in the experimental reports of No.1802 and No.1841. Note that in those experiments we used a good single crystal of $CoNb_2O_6$ prepared by the floating zone(FZ) technique, instead of the sample prepared by flux method, which is accompanied by extrinsic magnetic ordering due to crystal imperfection.

As a continuation of the proposal, we performed the neutron-diffraction measurements at the two-axis diffractometer E4 installed at the Berlin Neutron Scattering Center in the Helmholtz Centre Berlin for Materials and Energy, using transverse- as well as longitudinal- uniaxial pressure device so that we can provide access to the (*HK*0) scattering zone under applied vertical magnetic field to the *c* axis.

As is in the experimental reports of No. 1683, the uniaxial pressure dependence of the ratio γ along both the *a*- and *b*-axes were already measured but using the flux-sample with crystal imperfection. Therefore, in present experiment, changing the original plan of "uniaxial-stress control of magnetic domain-growth kinetics characteristic to ITL", we re-measured these up to 0.6 GPa using FZ-sample. Results shown in Fig.1 are qualitatively agree with these of flux-sample, but are quantitatively different, which are crucial to estimate the uniaxial pressure dependence of coupling constants J_1 and J_2 in combination with magnetic phase transition fields obtained by dc- and ac-susceptibility.

As shown in Fig.2(a1-a3), we also investigated temperature variation in the magnetic correlations at $\gamma \sim 1.3$ ($p_{\|c}$ = 0 MPa), $\gamma \sim 1$. ($p_{\|c}$ = 0.8 GPa) and $\gamma \sim 0.9$ ($p_{\|c}$ = 1.1 GPa) in detail. Because of unavoidable inhomogeneity of uniaxial pressure, at $p_{\|c} \sim 0.8$ GPa ($\gamma \sim 1$), AF-I and AF-II magnetic LRO coexist so that unfortunately we were not able to investigate magnetic correlations specific to Wannier point (γ = 1) at the lowest temperature. As shown in Fig.2(b), however, the temperature dependence of propagation wavenumber q of sinusoidally-amplitude- modulated incommensurate (IC) state at specific γ is qualitatively consistent with Stephenson's exact calculation for 2D isosceles triangular lattice Ising antiferromagnet.

In contrast to that both AF-I and AF-II magnetic orderings coexist at $p_{\|c} \sim 0.8$ GPa ($\gamma \sim 1$) as is seen in Fig.3(a), almost flat diffraction profile can be seen at $p_{\|b} \sim$ 0.6GPa ($\gamma \sim 1$) as shown in Fig.3(b), suggesting good "spot" to investigate field-induced magnetic states specific to Wannier point (γ = 1) . Further beam experiments are desired.

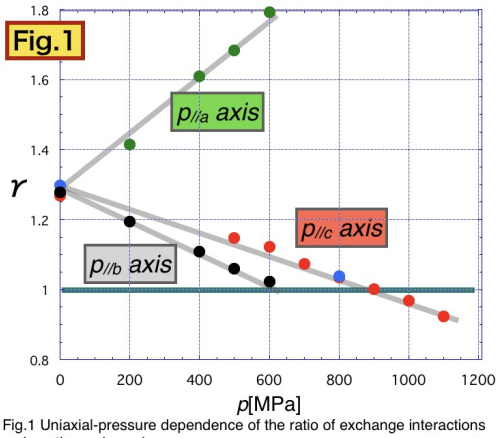

Fig.1 Uniaxial-pressure dependence of the ratio of exchange interactions γ along the a-, b- and c- axes.

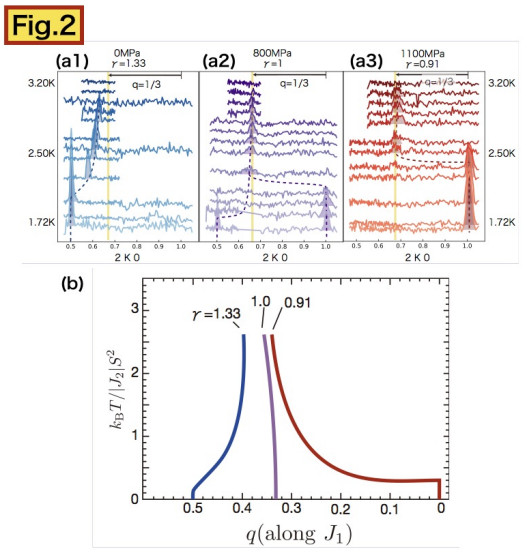

Fig.2 Temperature dependence of (2 k 0) scan profiles in zero magnetic field at (a1) γ~1.33 ($p_{//c}$=0GPa), (a2) γ~1.0 ($p_{//c}$=0.8GPa) and (a3) γ~0.9 ($p_{//c}$= 1.1GPa), respectively. (b) Temperature variation of propagation wavenumber q of short range magnetic correlation at specific γ, which is obtained from Stephenson's exact calculation for 2D isosceles triangular lattice Ising antiferromagnet.

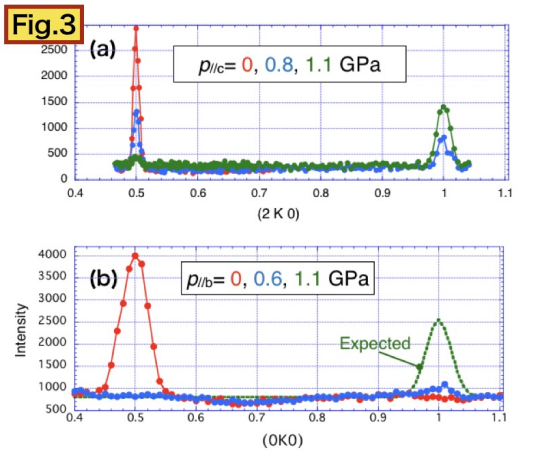

Fig.3 (a) (2 k 0) scan profiles in zero magnetic field at T=1.7K and $p_{//c}$= 0, 0.8 and 1.1GP , (b) (0 k 0) scan profiles in zero magnetic field at T=1.7K and $p_{//b}$= 0, 0.6 and 1.1 GP.

Fig. 1.

Determination of the Magnetic Structure under Magnetic Field of the Noncentrosymmetric Heavy-Electron Metamagnet $CePtSi_3$

Daichi Ueta, Yoichi Ikeda[B], Takatsugu Masuda, and H. Yoshizawa
ISSP-NSL, the University of Tokyo, IMR, Tohoku University[B]

Non-centrosymmetric *f*-electron materials have attracted much attention because the lack of inversion symmetry leads to significant and interesting physical properties. Recently, we observed that the non-centrosymmetric $BaNiSn_3$-type compound, $CePtSi_3$, exhibits successive magnetic transitions, multiple metamagnetic transitions, yielding an unusually complex $H - T$ phase diagram. We defined three phases (III, II and I) at elevated temperature. From elastic neutron diffraction experiments at zero field performed last summer, we found that the magnetic peaks observed at the commensurate position in phase III and at the incommensurate position in phase I. In addition, the *h*- and *k*-domains coexist in $CePtSi_3$ at zero field.

In order to determine magnetic structures in $CePtSi_3$ under fields in the next step, we performed elastic neutron scattering experiments at BL-09 (CORELLI), SNS in Oak Ridge National Laboratory. A single crystalline sample of $CePtSi_3$ was grown using a flux method at the Institute for Solid State Physics. The sample was mounted on a Cu pin such that both the *a*- and *c*-axes set into the equatorial plane and installed in SlimSam. Temperature was set to 1.8 K, and a magnetic-field was applied from 0 to 50 kOe along the *h*-direction (the *a*-axis).

We succeeded in observing clear and interesting field-dependence of magnetic peaks (Figure 1). It was suggested that the field region from 5 to 20 kOe can be classified into two phases. The *k*-domain in the magnetic field region of 5 to 14 kOe is still in the commensurate phase, but the *h*-domain changes to the incommensurate phase, and its magnetic propagation vector, q_{2h}, changes from 0.283 to 0.31 and the scattering intensity decrease sharply. In the magnetic field region from 14 to 20 kOe, the *h*-domain saturates at q_{2h} = 0.31, and the scattering intensity of magnetic peaks further decreases and disappears at 20 kOe. On the other hand, in the *k*-domain at 14 to 20 kOe, an incommensurate phase of q_{1k} = 0.283 appears, which is a crossover region between the incommensurate and commensurate phase. Finally, all magnetic superlattice peaks disappear above 45 kOe because of forced ferromagnetism. We are in the process of determining the mechanism of such magnetic structures in field. Travel expenses were supported by General User Program for Neutron Scattering Experiments, Institute for Solid State Physics, The University of Tokyo (proposal no. 18508), at JRR-3, Japan Atomic Energy Agency, Tokai, Japan.

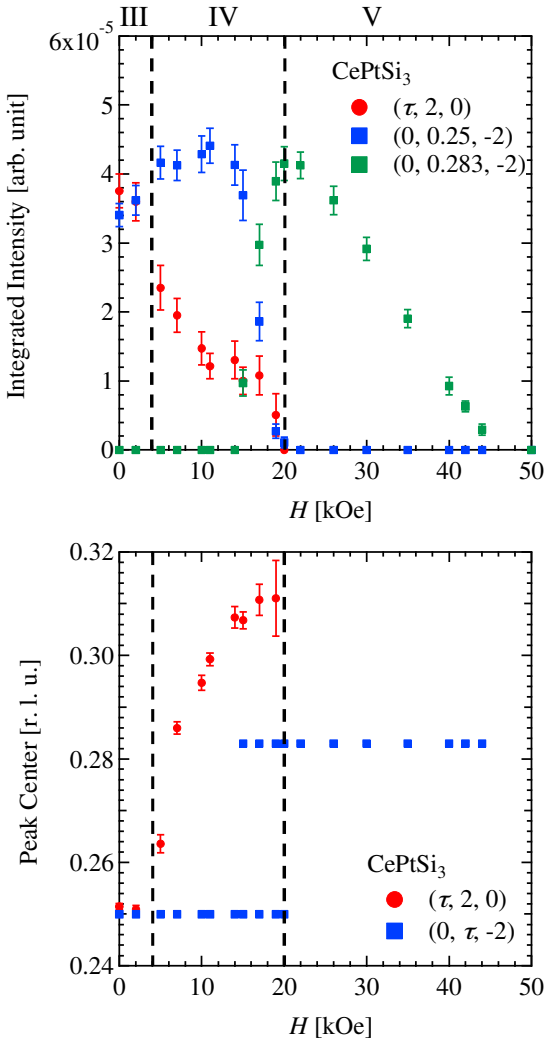

Fig. 1. Magnetic field dependence of the integrated intensity and peak position related to propagation vectors in *h*- and *k*-domains.

Spin excitations in the magnetic skyrmion-lattice phase

Seno Aji, Shinichiro Yano(A), and Taku J Sato
IMRAM, Tohoku University, (A) NSRRC

MnSi attracts renewed interest because of the recent discovery of the magnetic skyrmion-lattice structure under finite magnetic field [1]. The magnetic skyrmion is a topological spin texture made of swirling magnetic moments. The magnetic skyrmion carries integer topological number, called skyrmion number. In the real magnets, such as MnSi, the skyrmion forms a triangular lattice. The elementary excitation of ordered magnet is "magnon", which is a propagating quantized wave of spin fluctuations. The magnon would exists in the skyrmion-lattice phase, forming magnon bands with the Brillouin zone set by the periodicity of the triangular lattice. In addition, the topological nature of the scatterers (i.e. skyrmions) will give rise to non-trivial characters to the magnon bands, forming the topological magnon band [2]. Such a topological magnon is of current interest and are under active scrutiny, recently.

In search for the topological magnons, it was necessary to use Ge-doped MnSi, as Ge-doping increases the magnetic modulation vector k, relaxing Q-resolution requirement for the experiment. A single crystal sample $MnSi_{0.98}Ge_{0.02}$ of 15.5 grams was grown using Bridgman method. We performed elastic and inelastic neutron scattering using the cold-neutron triple-axis spectrometer SIKA, ANSTO. The collimations were Open-20'-20'-60' with vertically focusing monochromator. The final neutron energy was fixed to 2.75 meV. Pyrolytic graphite 002 reflections were used for monochromator and analyzer. The sample was mounted on the aluminum plate, aligned with 110 and 001 in the scattering plane. The vertical superconducting magnet was used in the experiment, applying external magnetic field along the $\bar{1}10$ direction.

From elastic neutron measurement, we obtained the modulation vector and the helical ordering temperature as $k = 0.0462$ Å^{-1} and $T_c = 32$ K, respectively. The obtained modulation vector and the helical ordering temperature are larger compared to MnSi ($k = 0.036$ Å^{-1} and $T_c = 29.5$ K). In the inelastic neutron measurement, the magnetic excitation in the skyrmion-lattice phase was measured at Γ, M, and their midpoint at $T = 30.5$ K and $H = 0.2$ T. Shown in the figure is the representative magnetic excitation spectrum observed at the midpoint. Broad inelastic peak can be seen around $\hbar\omega \sim 0.13$ meV. We confirmed that this excitation is intrinsic in the skyrmion-lattice phase, by comparing it to the excitation spectra both in the fully-polarized and helical phases. Detailed analysis, including theoretical estimation of the magnon scattering intensity in the skyrmion-lattice phase, is in progress.

[1] S. Mühlbauer *et al*. Science 323, 915-919 (2009); [2] K. A. van Hoogdalem *et al*., Phys. Rev. B 87, 024402 (2013).

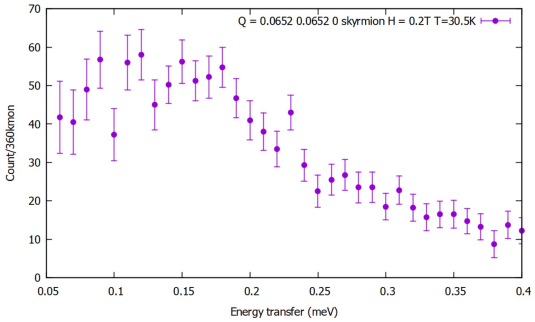

Fig. 1. Neutron inelastic spectrum at the mid point of the Γ and M points observed in the magnetic skyrmion-lattice phase

Neutron diffraction study on the Pd-Ga-Tb 2/1 quasicrystal approximant

Taku J. Sato, Maxim Avdeev(A), Kyohei Takagi(B), and Yeong-Ge So(B)
IMRAM, Tohoku University, (A)ANSTO, (B)Akita University

Quasicrystal is a substance with long-range quasiperiodic atomic arrangement, nonetheless, with the rotational symmetry that is prohibited in the periodic crystals, such as the five-fold symmetry. The quasicrystal is, therefore, different from periodic crystals and random glasses, and now is regarded as the third form of solids. There is a class of crystals, called "approximants", in which the high-symmetry (such as icosahedral) atomic clusters, identical to those in the quasicrystals, form periodic array, and thus being approximation of the quasicrystalline structure. The degree of approximation is expressed by the fractional numbers, such as 1/1 and 2/1. The 1/1 approximant is the lowest order approximation, in which the atomic clusters form a bcc cubic lattice. The 2/1 approximant has a larger unit cell, becoming a better approximation to the quasicrystal. As the fractional number becomes the irrational golden ratio $\tau \sim 1.618...$, the unit cell becomes infinitely large, i.e. quasicrystal.

Recently, for the first time we have determined magnetic structure of the antiferromagnetic 1/1 Au-Al-Tb approximant using ECHIDNA [1], which turns out to be a very intriguing non-collinear and non-coplanar whirling order. Quite recently, one of the proposers further found a magnetic 2/1 approximant in the Ga-Pd-Tb system, which orders antiferromagnetically at 5.8 K [2]. This is definitely the first 2/1 approximant that shows antiferromagnetic long-range order, which excites us enough to perform this neutron powder diffraction study.

A polycrystalline alloy of the Pd-Ga-Tb 2/1 approximant was prepared by arc melting with high purity ($>$ 99.9 wt%) Pd, Ga and Tb elements. The neutron powder diffraction experiment has been performed using the high-resolution powder diffractometer ECHIDNA installed at the OPAL reactor, Australian Nuclear Science and Technology Organisation [3]. For most of the magnetic diffraction measurement, neutrons with $\lambda = 2.4395$ Å was selected using the Ge 311 reflections, whereas for the structure analysis, to obtain reflections in a wide Q-range, we select $\lambda = 1.622$ Å using the Ge 335 reflections. The sample was set in the $\phi 6$ mm vanadium sample can, and then set to the cold head of the closed cycle ^{4}He refrigerator with the base temperature 3.5 K.

Figure shows the overall diffractograms at various temperatures ranging from the base ($\simeq$ 3.5 K) to the paramagnetic temperature 7 K. One can clearly see the development of sharp magnetic reflections below 5 K. They are the clear indication of magnetic long-range order in this 2/1 approximant. We further note that the magnetic reflection appearing at $2\theta \simeq 21.9$ degrees is relatively weak, compared to that observed in the Au-Al-Tb 1/1 approximant [1]. On the other hand, quite a few magnetic reflections can be seen in the Pd-Ga-Tb 2/1 approximant, number of which is much larger than that in the Au-Al-Tb 1/1 approximant. These results suggest that the magnetic structure would be much more complicated in the Pd-Ga-Tb 2/1 approximant, and is of significant interest in view of larger unit cell of the 2/1 approximant. The magnetic structure analysis using the representation analysis is in progress.

[1] T. J. Sato *et al.* (submitted); [2] Y. -G. So *et al.* (in preparation); [3] M. Avdeev and J. R. Hester, J. Appl. Crystallogr. 51, 1597 (2018).

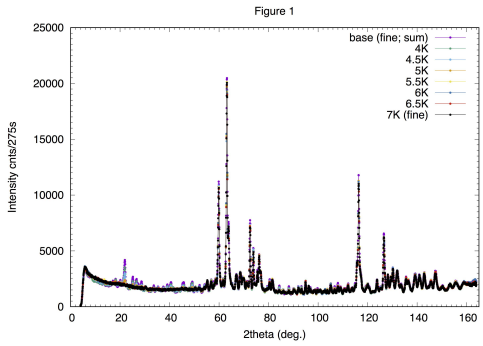

Fig. 1. Neutron diffraction patterns obtained in the temperature range $4 < T < 7$ K at ECHIDNA.

Neutron diffraction study on the $Yb_3Ru_4Al_{12}$ itinerant kagome antiferromagnet

Taku J Sato, Noriyuki Kabeya(A), Maxim Avdeev(B), Shintaro Nakamura(C), and Akira Ochiai(A)
IMRAM Tohoku University, (A)Dept. Phys. Tohoku University, (B)ANSTO, and (C)IMR Tohoku University

Geometrically frustrated spin systems have been studied extensively for decades because of many intriguing phenomena, exemplified by the non-magnetic quantum disordered states. Despite a large number of both experimental and theoretical studies, the ground states and excitations in geometrical frustrated quantum magnets are still largely unrevealed. This is the case for kagome compounds where even theoretically the ground state is controversial with gapped (such as Z2 spin liquid) or gapless (U(1) Dirac spin liquid) states. Experimentally, on the other hand, due to the small number of model compounds, the work is further less conclusive, and much efforts have been devoted to find out new model materials possessing the geometrically frustrated lattices. Recently, a new direction has been taken to discover new frustrated systems in Yb^{3+} rare-earth ions; several reports indicate quantum nature of the Yb^{3+} rare-earth magnetism, such as spinon continuum in quasi-one-dimensional Yb_4As_3 [1] and Yb_2Pt_2Pb [2]. The key ingredient of such quantum spin formation is doubly degenerated ground states (pseudo spin 1/2) made of strongly coupled L and S. Hence, there now appears a chance to study geometrically frustrated quantum magnetism using Yb-based compounds. The present proposer group found a Yb^{3+} based compound $Yb_3Ru_4Al_{12}$ [3], which has an archetypal frustrated lattice, called breathing kagome lattice. This compound shows intriguing low-dimensional frustrated behavior [3], and hence, we have investigated microscopic magnetism using powder neutron diffraction.

A polycrystalline alloy of $Yb_3Ru_4Al_{12}$ was prepared by crushing the single crystals. The neutron powder diffraction experiment has been performed using the high-resolution powder diffractometer ECHIDNA installed at the OPAL reactor, Australian Nuclear Science and Technology Organisation [4]. For most of the magnetic diffraction measurement, neutrons with $\lambda = 2.4395$ Å was selected using the Ge 311 reflections, whereas for the structure analysis, to obtain reflections in a wide Q-range, we select $\lambda = 1.622$ Å using the Ge 335 reflections. The sample was set in the ϕ4 mm Cu sample can, and then set to the cold head of the ^{3}He one-shot-type refrigerator with the base temperature 0.37 K. For the high-T (6.5 K), base-T and intermediate-T ($T_{\rm set} = 1.6$ K) scans, the total data acquisition time was 15 hours.

Figure shows the comparison of the diffraction patterns in the 2θ-range of $10 < 2\theta < 60$ degrees observed at the three temperatures. Clearly, magnetic signal develops at $2\theta \simeq 15^\circ$ and 18.5° at low temperatures. We note that $2\theta \simeq 15^\circ$ corresponds to the (0,0,1) (forbidden) nuclear reflection position, indicating that the magnetic structure is antiferromagnetic along the c-axis. The 18.5° peak corresponding to the (1,0,0) position. While magnetic signal was clearly observed in the low temperature phase, the nature of the intermediate phase is still unclear, but some hints may be obtained by carefully analyzing the present dataset. Magnetic structure analysis of the base-temperature phase is in progress, while we look for a way to elucidate nature of the intermediate phase, too.

[1] M. Kohgi, K. Iwasa, J.-M. Mignot, A. Ochiai, and T. Suzuki, Phys. Rev. B 56, R11388 (1997); [2] L. S. Wu, W. J. Gannon, I. A. Zaliznyak, A. M. Tsvelik, M. Brockmann, J.-S. Caux, M. S. Kim, Y. Qiu, J. R. D. Copley, G. Ehlers, A. Podlesnyak, and

M. C. Aronson, Science 352, 1206 (2016); [3] S. Nakamura, S. Toyoshima, N. Kabeya, K. Katoh, T. Nojima and A. Ochiai, Phys. Rev. B 91, 214426 (2015); [4] M. Avdeev and J. R. Hester, J. Appl. Crystallogr. 51, 1597 (2018).

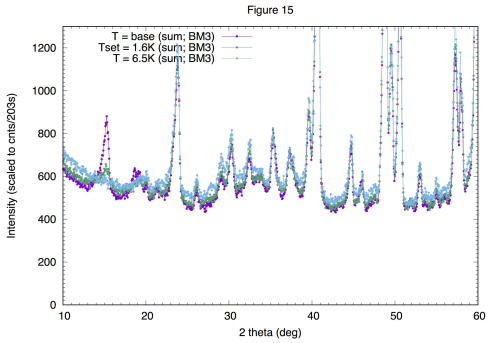

Fig. 1. Neutron diffraction patterns at the base temperature, 1.6 K and 6.5 K obtained at ECHIDNA. The temperatures are the “set” temperatures, and actual temperatures were slightly lower.

Dynamics of the magnetic skyrmion under an alternative current in MnSi

D. Okuyama(A), M. Bleuel(B), Q. Ye(B), A. Kikkawa(C), Y. Taguchi(C), Y. Tokura(C,D)
D. Higashi(A), J. D. Reim(A), Y. Nambu(E), and T. J. Sato(A)
(A)IMRAM, Tohoku Univ., (B)NCNR, NIST, (C)RIKEN-CEMS, (D)Univ. of Tokyo, (E)IMR, Tohoku Univ.

A magnetic skyrmion is swirling spin texture characterized by a discrete topological number, called the skyrmion number. In experiment, magnetic skyrmions quite often condensate in the triangular-lattice form, giving rise to six-fold magnetic Bragg reflections in small angle neutron scattering (SANS) patterns, as first discovered by Muhlbauer et al. in the prototypical chiral magnet MnSi [1]. To date, the skyrmion lattice structures are widely confirmed in various magnets ranging from metallic to insulating compounds. There are several prominent characteristics in magnetic skyrmions that make them quite intriguing. One of such characteristics is its topological protection; once created, the skyrmion can hardly be annihilated. In metallic skyrmion compounds, there is another important characteristic, i.e., its surprisingly large coupling with the electric current flow. The electric current density required to realize the skyrmion lattice motion is considerably small as j ˜ 1 MA/m2 [2]. Hence, the magnetic skyrmion attracts growing attention recently, and is under intense scrutiny for elucidating its dynamical behavior under electric current.

To investigate the dynamics of the magnetic skyrmion lattice under the electric current flow, we performed SANS experiment with suppressing the thermal gradient as much as experimentally achievable. SANS experiments were carried out at NG7 (National Institute of Standards and Technology). The incident neutron wave- length was selected using the velocity selector as λ i = 6 . An direct or alternative electric current with square wave was applied along the [0 0 1] direction. The sample mount was attached to the sample stick, and was installed in the horizontal field magnet with the magnetic field applied along [1 -1 0] parallel to the incident neutron beam.

We observed the six-hold magnetic skyrmion reflections at 28.6 K, respectively, under B = 0.2 T and j = 0 MA/m2. By comparing to SANS data at j = 0, one can clearly see considerable broadening of the skyrmion-lattice peaks in the azimuthal direction. The peak broadening is apparently temperature dependent; the width is considerably larger at T = 28.3 K compared to that at T = 28.6 K. This result clearly indicates significant deformation of the skyrmion lattice under large electric current. To investigate the origin of the broadening of the skyrmion reflections, we performed SANS measurements on the left-edge (+) or right-edge (-) of the sample. The size of the neutron illumination area is approximately 0.2 mm (width) × 1.0 mm (height). The observed patterns are identical for the two edges. In marked contrast to the zero-current condition, under j = 2.7 MA/m2 the reflection patterns taken from the left- and right-edge parts exhibit counterclockwise and clockwise rotations, respectively. The effect of inverting the current and magnetic-field directions was also investigated. The rotation direction does not change by inverting the magnetic field direction. On the other hand, the inversion of the current direction (from j = +2.7 to -2.7 MA/m2) results in a sign change of the rotation angle. This indicates that the skyrmion-lattice rotation observed in the thermally homogeneous condition depends not on the magnetization direction, but only on the current direction [3]. To observe the time dependence of the magnetic skyrmion rotation, we also performed the SANS experiment with applying the alter-

native electric current. The observed relaxation time of the skyrmion rotation is several seconds order, which is the very slow dynamics as a magnetic material.

In summary, we have used SANS to study skyrmion-lattice motion in bulk MnSi under electric current flow. The azimuthal width of the skyrmion-lattice peaks shows significant broadening above a threshold current density jt ˜ 1 MA/m2. We show this peak broadening originates from a spatially inhomogeneous rotation of the skyrmion lattice, that shows opposite senses of rotation at the sample edges.

Reference:

[1] S. Muhlbauer, B. Binz, F. Jonietz, C. Pfleiderer, A. Rosch, A. Neubauer, R. Georgii, and P. Boni, Science 323, 915 (2009).

[2] F. Jonietz, S. Muhlbauer, C. Pfleiderer, A. Neubauer, W. Munzer, A. Bauer, T. Adams, R. Georgii, P. Boni, R. A. Duine, K. Everschor, M. Garst, and A. Rosch, Science 330, 1648 (2010).

[3] D. Okuyama, M. Bleuel, J.S. White, Q. Ye, J. Krzywon, G. Nagy, Z.Q. Im, I. Zivkovic, M. Bartkowiak, H.M. Ronnow, S. Hoshino, J. Iwasaki, N. Nagaosa, A. Kikkawa, Y. Taguchi, Y. Tokura, D. Higashi, J.D. Reim, Y. Nambu, and T.J. Sato, accepted in Commun. Phys.; arXiv:1807.07388.

Determination of the spin system in $Ni_2V_2O_7$ using neutron diffraction in magnetic fields

Masashi Hase Matsuo[1], James R. Hester[2], and Kirrily C. Rule[2]
[1]*National Institute for Materials Science (NIMS),* [2]*Australian Nuclear Science and Technology Organisation (ANSTO)*

Neutron diffraction has made great contribution to studies of magnetism because magnetic structures can be determined. We can also study magnetism in paramagnetic states by combing neutron diffraction and magnetic fields. Magnetic moments are induced by magnetic fields and generate magnetic reflections. In a magnet with plural crystallographical magnetic-ion sites, we can evaluate a field-induced magnetic moment (magnetization) on each site from analyses of the magnetic reflections.

Our objective in this study is to show that neutron diffraction in magnetic fields is a powerful tool to determine spin systems. We investigated $Ni_2V_2O_7$ as an example. We briefly summarize the magnetism of $Ni_2V_2O_7$ [1]. Magnetic phase transitions occur at $T_{N1} = 6.7$ and $T_{N1} = 5.7$ K. The magnetic structures have not been determined. A 1/2 quantum magnetization plateau was observed between 8 and 30 T at 2 K. There are two crystallographical Ni^{2+}-ion sites having spin-1. There are three types of short Ni-Ni pairs having antiferromagnetic exchange interactions. A few sets of the values were reported and were inconsistent with one another [1,2].

In order to determine the spin system (the values of the exchange interactions) in $Ni_2V_2O_7$, we performed neutron diffraction experiments on $Ni_2V_2O_7$ pellets using the WOMBAT diffractometer and the AVM-1 magnet. We can see several magnetic reflections in a difference pattern made by subtracting a neutron powder diffraction pattern at 10 K in 0 T from that at 1.8 K in 0 T. We infer an incommensurate magnetic structure from the positions of the magnetic reflections.

Figure 1 shows a difference pattern made by subtracting a neutron powder diffraction pattern at 20 K in 10 T from that at 1.8 K in 10 T. As described, the 1/2 quantum magnetization plateau appears above 8 T at low temperature. Therefore, the state at 1.8 K in 10 T is a kind of paramagnetic state (without magnetic long-range order). We can see several magnetic reflections generated by field-induced magnetic moments. The red circles indicate intensities of magnetic reflections calculated in the case that M2/M1 = 5. Here, M1 and M2 are the magnitude of field-induced magnetic moments on Ni1 and Ni2 sites, respectively. The calculated intensities seem consistent with the experimental ones. Several reflections indicated by triangles, however, cannot be explained by the field-induced magnetic moments. The magnetic reflections at 1.8 K in 0 T seem to remain, suggesting the coexistence of the two phases.

We measured difference patterns at 1.8 K in several magnetic fields. As the magnetic field increases, the intensities of the magnetic reflections at 1.8 K in 0 T and those generated by field-induced magnetic moments decrease and increase, respectively. We can see magnetic reflections that are different from those in 0 and 10 T at 1.8 K. Probably, the indices of the magnetic reflections are integers. The intensity of the magnetic reflections increases with increasing magnetic field and is strongest around 6 to 8 T, suggesting another magnetic long-range order in finite magnetic fields below the magnetization-plateau fields. The magnetic reflections disappear in 10 T.

We will determine the magnetic structures in zero and finite magnetic fields and evaluate M1 and M2 at 1.8 K in 10 T. We will be able to determine the spin system

(the values of the exchange interactions).

[1] Z. W. Ouyang et al., Phys. Rev. B. 97, 144406 (2018).

[2] Y. C. Sun et al., Eur. Phys. J. Plus 131, 343 (2016).

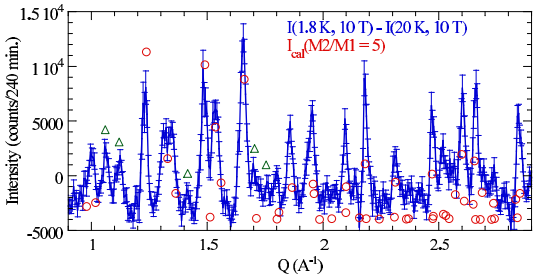

Fig. 1. A difference pattern made by subtracting a neutron powder diffraction pattern at 20 K in 10 T from that at 1.8 K in 10 T.

Full control of magnetic moment in multiferroics Ba2CoGe2O7

Shunsuke Hasegawa and Takatsugu Masuda
ISSP, the University of Tokyo

Electric control of magnetic moment is an intriguing topic in condensed mater physics since it can be applied to a novel device. Coexistence of magnetic order and electric polarization, multiferroicity, has a possibility to realize such a control. So far spin helicity was controlled in $TbMnO_3$ [1] and magnetic domain was controlled in Hexaferrite [2], but controlling local magnetic moment by applying electric field has not been demonstrated yet. $Ba_2MGe_2O_7$ (M = Co, Mn) are multiferroic compounds with spin-dependent $p-d$ hybridization mechanism [3]. The crystal structure is a tetragonal and the space group is P-421m. Below T_N = 6.7 K, the spin antiferromagnetically lies along the crystallographic a axis, and the electric polarization antiferroelectrically lies along the c axis. It is expected that the applying electric field along the c axis changes the antiferroelectric state to ferroelectric state with the magnetic moment rotating from [100] to [110]. Soda et al. demonstrated the rotation of the magnetic moment in the ab plane [4], but the moment did not make complete rotation by 45 degrees due to a large in-plane magnetic anisotropy. It was only 6 degrees at T = 1.5 K and E = 1.5 MV/m at best. Then we performed a similar experiment on $Ba_2MnGe_2O_7$ [5] having smaller anisotropy energy at PSI. The rotation of the magnetic moment was observed at 1.5 K, and the angle as large as 20 degrees was achieved by increasing the temperature. The perfect rotation of 45 degrees was, however, not achieved because of the short of the electric field. It should be noted that a non-linear behavior was observed in the field dependence of the rotation angle, and a non-trivial plateau was found at 2 MV/m $<$ E $<$ 5 MV/m, even though a simple linear behavior was expected [4]. Even though the anisotropy energy of $Ba_2MnGe_2O_7$ is smaller than that of $Ba_2CoGe_2O_7$, the electric polarization is also smaller, resulting in the smaller rotation angle at the same electric field at the base temperature: 1.5 degree for $Ba_2MnGe_2O_7$ and 6 degrees for $Ba_2CoGe_2O_7$ at E = 1.5 MV/m. Use of $Ba_2CoGe_2O_7$ is better choice. We have done the Polarized Neutron Diffraction to achieve the perfect rotation by applying stronger electric field on thinner $Ba_2CoGe_2O_7$ sample and by reducing the anisotropy energy at high temperature. Then we tried to detect non-trivial field dependence of the rotation angle of the magnetic moment to understand. A single crystal sample was grown by the floating-zone method. The single crystal was aligned so that the crystallographic ab plane was in the horizontal plane. For the single crystal with a thickness of 2.65 mm, aluminum electrodes were deposited onto the faces of (001) to apply the electric field. The sample was set in the Al sample can, and then sample space was vacuumed. Maximum voltage in the used equipment was 7.0 kV. Heusler alloy was used to obtain the polarized neutrons with the energy of 13.5 meV. Magnetic Bragg peaks are observed below T_N. From the analysis of the peaks, it is found that the easy-plane type antiferromagnetic structure having a magnetic propagation vector $\mathbf{k}_{mag} = (0, 0, 0)$ is realized, which is consistent with the previous report [6]. Since the sample has crystallographic domains, we performed the $\theta - 2\theta$ scan at maximum point of omega scan in order to estimated integrated intensity. (h, k, l)= (2, 1, 0) and its equivalent reflections were measured to investigate the electric field and temperature dependence. We assume that the magnetic moments continuously rotate from [100] (or [010]) to [110] directions when the antiferroelectric state becomes the ferroelectric state retaining an-

tiferromagnetic structure by applying the electric field along the c axis as same as the previous report [4]. Under this assumption the intensity variation at (2, 1, 0) and its equivalent position is represented by the sinusoidal curve as follows:

$$I \propto 1 + \sin 2\theta \sin 2\omega \qquad (1)$$

where I is the intensity of each magnetic reflections, and the ω is a rotation angle of the magnetic moment from [100] or [010] to [110]. The θ is the angle between the scattering vector and a axis. The rotation angle of the magnetic moment is evaluated from the amplitude of the sinusoidal curve. Figure 1 shows electric field dependences of the normalized magnetic intensities as a function of θ at 1.5 K. Normalized magnetic intensities were got from intensities divided by the average of intensities which were evaluated from magnetic intensities divided nuclear intensities at same Q position. The data show a sinusoidal curve at each electric field like equation (1). The amplitude increases with increase of the electric field, which means that the rotation angle of magnetic moment increases with. From fitting the data by equation (1), we obtained the rotation angle of magnetic moment against the electric field at 1.5 K, 6.0 K and 6.3 K. At 1.5 K data, the rotation angle is almost consistent with previous report. The rotation angle at 6.0 K and 6.3 K was reproduced by the theoretical calculation at 1.5 K in previous study [4], even though we apply higher electric field. This means that the controllability of magnetic moment is independence of temperature. Furthermore, non-trivial field dependence of the rotation angle of the magnetic moment was not observed.

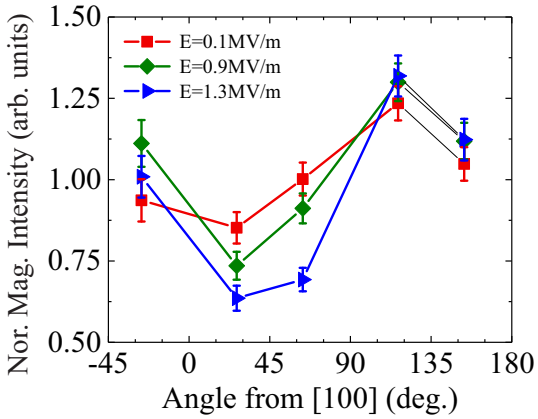

Fig. 1. Electric field dependences of normalized magnetic intensity at 1.5K.

[1] Y. Yamasaki et al., Phys. Rev. Lett. 98, 147204 (2007). [2] S. Ishiwata et al., Science 319, 1643 (2008). [3] H. Murakawa et al., Phys. Rev. B 85, 174196 (2012). [4] M. Soda et al., Phys. Rev. B 94, 094418 (2016). [5] T. Masuda et al., Phys. Rev. B 81, 100402 (2010). [6] A. Zheludev *et al*., Phys. Rev. B **68**, 024428 (2003).

Quantum spin liquid state of $Tb_{2+x}Ti_{2-x}O_{7+y}$

H. Kadowaki[A], B. Fåk[B], J. Ollivier[B], T. J. Sato[C]
[A]*Department of Physics, Tokyo Metropolitan University, Hachioji, Tokyo 192-0397*
[B]*Institute Laue Langevin, BP156, F-38042 Grenoble, France*
[C]*IMRAM, Tohoku University, Sendai*

Geometrically frustrated magnets have been actively studied in recent years [1]. These include classical and quantum spin systems on two-dimensional triangle [2] and kagome [3] lattices, and three-dimensional pyrochlore-lattice systems [4]. For classical systems, prototypes of which are the trianglar-lattice antiferromagnet [2] and the spin ice [5], many investigations have been performed for a few decades using a number of theoretical and experimental techniques [1]. Possibilities of quantum spin liquid (QSL) states in frustrated magnets, which date back to the theoretical proposal of the RVB state [6], are recently under hot debate. Highly-entangled many-body wave functions without magnetic long-range order (LRO), anticipated in QSL states, provide theoretically challenging problems [7]. Experimentally, finding out real QSL substances, e.g. [8], and investigating QSL states using available techniques, e.g. [9], have been attracting much interest. However, to date, nobody has found clear evidence of a QSL state, despite many trial experiments performed in the past decade [7,9].

A non-Kramers pyrochlore system $Tb_2Ti_2O_7$ (TTO) has attracted much attention since an interesting report of absence of magnetic LRO down to 0.1 K [10], which could be interpreted that TTO is a QSL candidate or quantum spin ice (QSI) [11]. On the other hand, a phase transition at $T_c \sim 0.5$ K detected by a specific heat peak suggesting a hidden LRO [12], seemed to contradict with the QSL interpretation. We resolved this contradiction by showing that ground states of TTO are highly sensitive to off-stoichiometry, i.e., x (and/or y) of $Tb_{2+x}Ti_{2-x}O_{7+y}$ [13], and that there are two ground states: an electric quadrupole ordered (QO) state ($x > x_c \sim -0.0025$) and the putative QSL state ($x < x_c$) [14] (Fig. 1 inset).

We now think that the QO state proposed in Ref. [14] or its variant likely account for the hidden LRO of TTO. On the other hand, the long-standing question of "what is the putative QSL state of TTO?" or even a simpler question of "is it really a QSL state?" are still difficult problems for present-day experimental techniques, which are not well optimized for studying QSL states. For example, in Fig. 1 we show inelastic neutron scattering (INS) spectra of TTO samples carried out at 0.1 K on IN5 and AMATERAS, which are normally known as good-energy-resolution spectrometers [16]. The energy spectrum of the QSL powder sample with $x = -0.005$ shown in Fig. 1 looks as though there are both elastic and inelastic scattering contributions. However, if this sample is in a QSL state at 0.1 K, this elastic scattering should be (at least partly) inelastic scattering with a very small energy scale [17,18].

Recently we proposed to perform INS experiments on $x = -0.005$ (QSL) and 0.005 (QO) powder samples using the extremely good energy-resolution ($\Delta E \sim 1$ μeV) spectrometers IN16B and HFBS, which have not commonly been used for studies of QSL states. Thereby, we have a good chance to observe that the seemingly elastic scattering shown in Fig. 1 is (partly) inelastic scattering, which consequently proves that the putative QSL TTO sample is definitely in a QSL state at $T = 0$. In addition, by simply comparing quasi-elastic spectra of the QSL and QO samples, distinct difference due to the two ground states can be we observed. We performed an ILL-DDT

experiment (2018 May) of the QSL sample using IN16B, which shows interesting experimental data. However an NCNR-QAP experiment (2018 Aug.) of the QO sample using HFBS was not successful owing to large instrumental background. Now we are waiting for another experiment of the QO sample using DNA (J-PARC) to answer the questions.

[1] C. Lacroix et al. Introduction to Frustrated Magnetism (Springer, Berlin, Heidelberg, 2011).
[2] G. H. Wannier, Phys. Rev. 79, 357 (1950).
[3] I. Syôzi, Prog. Theor. Phys. 6, 306 (1951).
[4] J. S. Gardner et al. Rev. Mod. Phys. 82, 53 (2010).
[5] S. T. Bramwell and M. J. P. Gingras, Science 294, 1495 (2001).
[6] P. W. Anderson, Mater. Res. Bull. 8, 153 (1973).
[7] L. Savary and L. Balents, Rep. Prog. Phys. 80, 016502 (2017).
[8] K. Hirakawa, H. Kadowaki, K. Ubukoshi, J. Phys. Soc. Jpn. 54, 3526 (1985).
[9] B. Fåk et al. Phys. Rev. B 95, 060402 (2017); Y. Shen et al. Nature 540, 559 (2016); Z. Zhu et al. Phys. Rev. Lett. 119, 157201 (2017).
[10] J. S. Gardner et al. Phys. Rev. Lett. 82, 1012 (1999).
[11] H. R. Molavian et al. Phys. Rev. Lett. 98, 157204 (2007).
[12] N. Hamaguchi et al. Phys. Rev. B 69, 132413 (2004).
[13] T. Taniguchi, H. Kadowaki, B. Fåk, J. Ollivier et al. Phys. Rev. B 87, 060408(R) (2013).
[14] H. Takatsu, S. Kittaka, A. Kasahara, Y. Kono, T. Sakakibara, Y. Kato, S. Onoda, B. Fåk, J. Ollivier, J.W. Lynn, T. Taniguchi, M. Wakita, H. Kadowaki, Phys. Rev. Lett. 116, 217201 (2016).
[15] M. Wakita, T. Taniguchi, H. Edamoto, H. Takatsu, H. Kadowaki, J. Phys. CS 683, 012023 (2016).
[16] H. Kadowaki, M. Wakita, B. Fåk, J. Ollivier, S. Ohira-Kawamura, K. Nakajima, H. Takatsu, M. Tamai, J. Phys. Soc. Jpn. 87, 064704 (2018); H. Kadowaki, M. Wakita, B Fåk, J. Ollivier, S. Ohira-Kawamura, K. Nakajima, J. W. Lynn, Phys. Rev. B 99, 014406 (2019).
[17] M. Hermele et al., Phys. Rev. B 69, 064404 (2004).
[18] C-J. Huang et al. Phys. Rev. Lett. 120, 167202 (2018); Y. Kato and S. Onoda, Phys. Rev. Lett. 115, 077202 (2015).

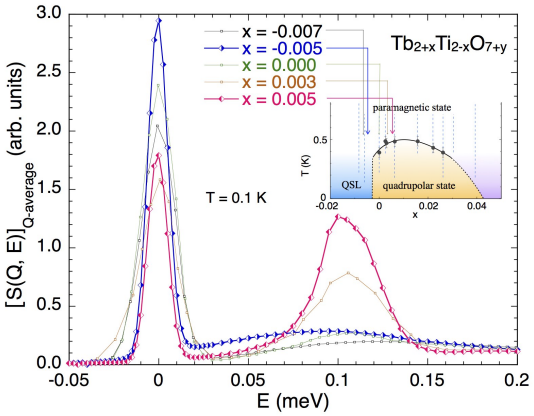

Fig.1 Energy spectra S(Q,E) averaged in a wide Q-range taken using crystal samples (x = -0.007, 0.000, 0.003) and powder samples (x = -0.005, 0.005) [16]. Inset shows the x-T phase diagram of Ref. [15].

Fig. 1.

Strongly Correlated Electron System

Investigation of vortex lattices on non-centrosymmetric superconductor LaNiC2

M. Soda, V. Ryukhtin, P. Strunz, and H. Furukawa
RIKEN, Nuclear Physics Institute, Ochanomizu University,

Non-centrosymmetric superconductor LaNiC2 attracts high interest in last decade due to rather unusual nature of superconductivity. It was supposed that lanthanum atoms participate to Cooper pair creation, because C is non magnetic and Ni magnetic contribution is practically zero [1]. Although, conventional superconductors can only have one spin states (either singlet or triplet) due to Pauli's principle and law of parity conservation, superconductors without inversion symmetry, however, can have a mixed spin states [2]. It was concluded from resistivity measurements at low T that the non-centrosymmetric compound LaNiC2 as a nonmagnetic and weakly-correlated superconductor with two-gap Bardeen-Cooper-Schrieffer.

We have used SANS-1 instrument installed at PSI for vortex lattice (VL) structure of mixed state in LaNiC2 measurements. Magnetic field H was applied along main crystal axes during the measurements. Angular scans were performed at 20 m from sample to detector. Wavelength was set to 12 \AA or 8 \AA depending on magnetic field value.

Structures of VL measured at H = 0.1 T is shown in Fig. 1. The data were collected with scanning over vertical axis by 0.2 degree, summed up, and corrected by background data collected using same scan.

The observed measurements show that vortex structure changes from triangle at H parallel to a-axis (Fig. 1(a)) to square lattice at H//c or H//b (Figs. 1(b) and 1(c)). One can see that VL structure is correlated with positioning of La atoms in orthorhombic cell for corresponded projection. The plane with lanthanum atoms (green spheres in Figs. 1 (d-f)) in triangular symmetry form triangular VL (Fig. 1 (a, d)) as it was measured by H//a. In case of orientations H//b, H//c lanthanum atoms arranged rectangular in plane perpendicular to H (Fig. 1(e), (f)) and resulted VL structures contain four spots.

Temperature dependencies of vortex spot intensities were measured for several magnetic fields in order to study important characteristic of superconductivity: coherence length, penetration depth, full gap/ nodal state and superconducting symmetry. At this moment, we try to analyze the data.

[1] P. Kotsanidis, J. Yakinthos, and E. Gamari-Seale: J. Less-Common Met. 152 (1989) 287.
[2] V.M. Edel'stein: Sov. Phys. JETP68 (1989) 1244.

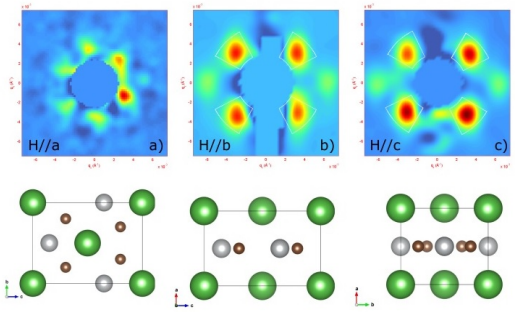

Fig. 1. VL as measured at 1000 Oe with magnetic field applied along main axis of LaNiC2 (a-c) and corresponding projection of crystal (d-f).

Investigation of magnetic ordering in high pressure phase of $DyMnO_3$

Noriki Terada(A), Navid Qureshi(B), Mechthild Enderle(B), Fabio Orlandi(C), Dmitry Khalyavin(C), Pascal Manuel(C) and Dharmalingam Prabhakaran(D)
(A)National Institute for Materials Science, (B)ILL, (C)ISIS and (D)University of Oxford

Abstract: In the experiments, we have succeeded in measuring the pressure dependence of the magnetic k-vector and polarization matrices of multiferroic $DyMnO_3$ under high pressure condition, by using the WISH TOF diffractometer and the CryoPAD apparatus on IN20 beamline in combination with our developed Hybrid-Anvil-Cell (HAC). This experiment determined the pressure dependence of some of neutron polarization matrices as well as magnetic propagation vector up to 5 GPa.

Unpolarized and polarimetry neutron experiments were carried out using WISH at ISIS and IN20 at ILL. Single crystal samples of $DyMnO_3$ for both the experiments, grown by the floating zone technique, were cut into rectangular shapes with dimension of 0.5 × 0.5 × 0.2 mm3 for experiments up to 5 GPa. The crystal qualities were kept even under pressure up to 5.0 GPa, by using glycerin as the pressure transmission medium. The cut samples were mounted in the HAC with the a-axis vertical, in order to provide access to the monoclinic (0, K, L) reflections. For the polarimetry experiment on IN20, the incident neutrons are polarized and monochromatized at the Heusler monochrometer. The incident wavelength 1.53 was employed. A sapphire anvil with a 2.4 mm diameter culet, supported by MP35N was used.

In the experiment on WISH and IN20 in July and September 2018, we succeeded in measuring the pressure dependence of k-vector and neutron polarization matrix up to 5 GPa. We could observe tendency that one of matrix elements, Pyy, significantly changes above 4 GPa, which indicates that Dy spin ordering gradually changes from spiral to collinear structure. However, in the previous experiments on IN20, due to limitation of machinetime, I have not measured the complete set of pressure dependence beyond 5 GPa.

In conclusion, we have determined the pressure dependence of the d-vector and polarization matrix elements. However, it is necessary to perform additional experiments to make this complete and clarify the magnetic ordering for higher pressure phase with the giant electric polarization in $DyMnO_3$.

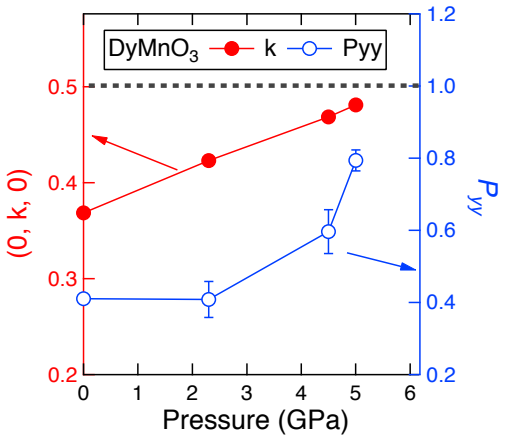

Fig. 1. Pressure dependence of propagation wave number k and polarization matrix element Pyy. The data were measured in the previous measurements on IN20.

Nesting features and the superconducting mechanism in Ce(Co,Rh)In5

Kanae Shinohara
Ochanomizu University

Heavy-fermion superconductor CeMIn5 (M=Co, Rh, Ir, tetragonal structure, space group P4/mmm) has been studied to understand relationship between the magnetism and the unconventional superconductivity. Neutron experiments revealed that CeCoIn5 (Tc ˜ 2.3 K) shows a resonance peak at (1/2 1/2 1/2) [1], and CeRhIn5 (TN ˜ 4K) has an incommensurate magnetic order with a propagation vector of q = (1/2, 1/2, 0.297) [2]. Mixed crystal CeRh1-xCoxIn5 in the middle x region possesses a commensurate magnetic order with the q = (1/2 1/2 1/2), and this requests that the superconductivity realized in the middle x region uses a different fermi surface if they use and that the resonance peak should move to some other q position.

To check the q position of the resonance peak in CeRh1-xCoxIn5 with the middle x region, we carried out an inelastic neutron scattering experiment. For this experiment, we prepared a co-aligned mosaic of the single crystals of CeRh0.6Co0.4In5 with the total volume ˜ 3 g with (h h l)-scattering plane because we expected that resonance peak would appear in q = (1/2, 1/2, l). Neutrons with Ei = 3.8 meV and Fermi chopper speed 240 Hz were used.We measured scattering data at 0.3 K, 2 K, 5 K, 50 K which correspond to the SC + AFM phase, tne AFM phase, normal phase, nomal phase at high temperature using for background, respectively. We are now analyzing data carefully.

This travel was done with a financial support by ISSP, University of Tokyo. We appreciate it pretty much since it could not be done without it.

References

[1] C. Stock et al., Phys. Rev. Lett. 100, 087001 (2008).
[2] W. Bao et al., Phys. Rev. B 62 (2000) R14621; Phys. Rev. B 67 (2003) 099903(E).

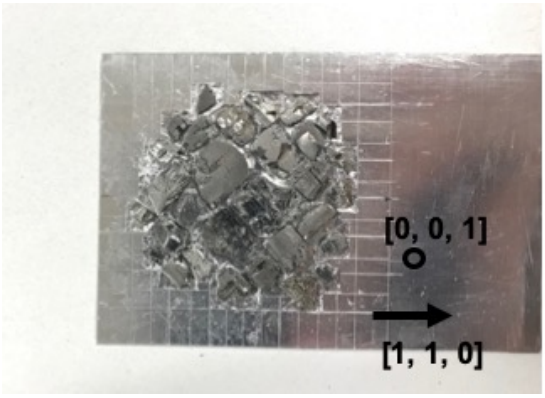

Fig. 1. Fig1. Co-aligned single crystals of CeRh0.6Co0.4In5

Biology

Elucidation of tri-ubiquitin dynamics concerning about status of interaction interfaces

Masaaki Sugiyama (A), Rintaro Inoue (A), Ken Morishima (A), Maho Yagi-Utsumi (B, C), Methanee Hiranyakorn (B, C), Michihiro Nagao (D), Hiroshi Nakagawa (E)
(A) Kyoto University, (B) National Institutes of Natural Sciences, (C) SOKENDAI, (D) NIST, (E) Japan Atomic Energy Agency

Ubiquitin is a small protein with 76 residues and regulates many functions in a cell: proteolysis, DNA-repair, post-translational modification, signal transduction and so on. The ubiquitin has a hydrophobic interface, and through the interface, the ubiquitin makes connection with a protein having ubiquitin-interaction motif. The functions depend upon which Lys-residue are used for the connection. When Lys48 is used for the connection, this poly-ubiquitin (K48 poly-ubiquitin) works as a degrading index of protein in a proteasome-ubiquitin system.

We investigated the structure and dynamics of K48 di-ubiquitin (K48-di-Ub) with NMR [1]. K48-di-Ubs are in an equilibrium and/or has transit dynamics between open and closed forms in solution. In the closed form, the activity of K48-di-Ub becomes low due to store of the interaction interface and, therefore, this conformational change regulates the ubiquitin functions. The aim of the NSE experiment is to reveal an inner domain motions between Ub domains in K48-tri-Ub in the closed and open forms. The equilibrium between the two conformations is dependent on temperature; the closed and open ones are dominant in the higher (42 degrees) and lower (10 degrees) temperature.

We measured NSE of K48-tri-Ub at the two temperature of 10 and 42 degrees at about 10 mg/ml. An incident neutron wavelength of 6 and 8 angstroms was used to cover fourier times up to 20 ns in a q-range from 0.06 to 0.22 inverse angstroms. Intermediate scattering functions for both states were successfully obtained. The effective diffusion constants (Deff) were obtained by exponential fittings at each q. Deff should include translational and rotational diffusion as well as internal domain motions. The experimentally obtained Deffs are consistent with the MD simulation derived ones at 10 degrees (see Fig.). Based on these results, the contribution of the internal motions can be estimated. The analysis on the temperature dependence of the internal dynamics is on progress. We are trying to analyze the NSE data combined with computational analysis to observe the functional domain motions of K48-tri-Ub.

Reference:
[1] T. Hirano, M. Yagi-Utsumi, K. Kato, et al., J. Biol. Chem., 286, 37496 (2011).

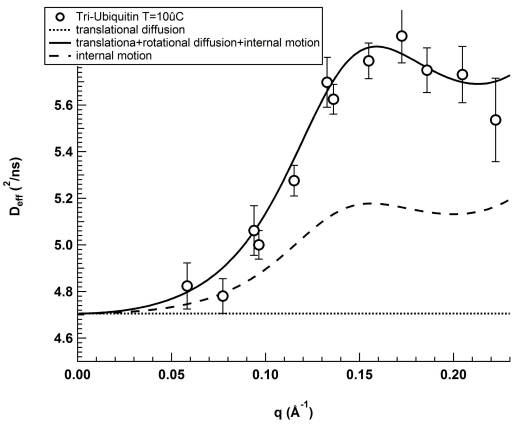

Fig. 1. Q-dependence of effective diffusion constants (Deff) from NSE experiment and MD simulation (translational diffusion, translational diffusion + rotational diffusion + internal motion, and internal motion).

Soft Matters

Solvent dependence in Platonic structures of resorcinarene-based capsule

Shota Fujii, Kazuo Sakurai
Department of Chemistry and Biochemistry, University of Kitakyushu

Resorcinarene-based amphiphiles including C-Methylresorcinarene and C-undecylresorcinaren (Figure 1a) self-assemble into spherical hexameric structures in apolar solvents such as chloroform and benzene.[1] The pioneer work for the characterization of the hexametric structure based on single-crystal X-ray diffraction was demonstrated by MacGillivray and Atwood in 1997.[1] The X-ray analysis was conducted for the single-crystal prepared from nitrobenzen, which elucidated the formation of a capsule-like structure consisting of 6 resorcinarene units and 8 water molecules with incorporating 60 hydrogen bonding. This resorcinarene-based hexameric capsule possesses high applied potential for catalysis carriers and still gets attention as interesting supramolecular aggregates.[2] The structural configuration of C-undecylresorcinarene capsule is associated with core-shell structures where undecyl-tails are placed on the surface on the core composed of hydrogen bonding network and solvent molecules, which might be categorized into reverse micelle structures.

As mentioned above, the structure of resorcinarene-based hexameric capsule has been clarified by single-crystal X-ray structural analysis. Though the way is extremely useful in elucidating the real structure in molecular level, the greatest problem is that the effects of environmental conditions such as various temperature and solvent composition on the aggregate structure are ignored when preparing single crystals. As an alternative method for visualizing the aggregate structure in solutions as it is, small angle neutron scattering (SANS) is very useful and can be conducted at the required experimental conditions (e.g. various temperature levels and solvent compositions). Atwood, Kumari , and coworkers have revealed that C-alkylpyrogallolarene, whose structure is almost identical with that of C-alkylresorcinarene, forms hexameric capsules with a core-shell geometry in chloroform by using SANS measurements.[3] The SANS study also have illuminated the structure of metal-organic pyrogallolarene-based capsules whose morphologies can be controlled by metal ion species. In this experiment, we investigate the solvent effect on the Platonic structure of C-undecylresorcinarene capsules using SANS measurements.

Figure 1b shows SANS profiles of C-undecylresorcinarene capsules in deuterated apolar solvent including toluene-d8 and chloroform-d. The scattering intensity approached to q0 at low-q region in the both systems, indicating the formation of spherical scatterers. The oscillation behaviors of the both profiles are similar to each other, but the q value at minimum position in toluene-d8 is larger than that in chloroform-d, indicating a difference in their structures. Since the inside of the C-undecylresorcinarene capsule contains the apolar solvent, and the large difference in the values of SLD between the deuterated solvents and the C-undecylresorcinarene molecule, we employed spherical hollow model as the fitting model where solvent molecules are located in the core. The fitting model could reproduce the experimental data, indicating the presence of solvent molecule in the capsule core. The size of the solvent pool in the capsule core in chloroform-d is almost consistent with reported value. However, it is relatively large compared to that in toluene-d8, which indicates the difference in the network structure through the hydrogen bonding among the hydroxyl groups in resorcinarene moiety and water molecules in each apolar

solvent. In toluene-d8, the full-stretched length of resorcinarene molecule (~1.6 nm) almost agree with that of shell thickness while the shell thickness in chloroform-d is smaller than the actual molecular size. This presumably suggests that the alkyl chains are flexibly mobile in the hexamric structure and efficiently cover the capsule core to minimize the interfacial free energy between the capsule core and the outer solvent.

[1] Leonard R. MacGillivray et al. Nature, 1997, 389, 469?472
[2] Qi Zhang et al. Acc. Chem. Res. 2018, 51, 2107 − 2114
[3] Harshita Kumari et al. J. Am. Chem. Soc., 2011, 133, 18102?18105

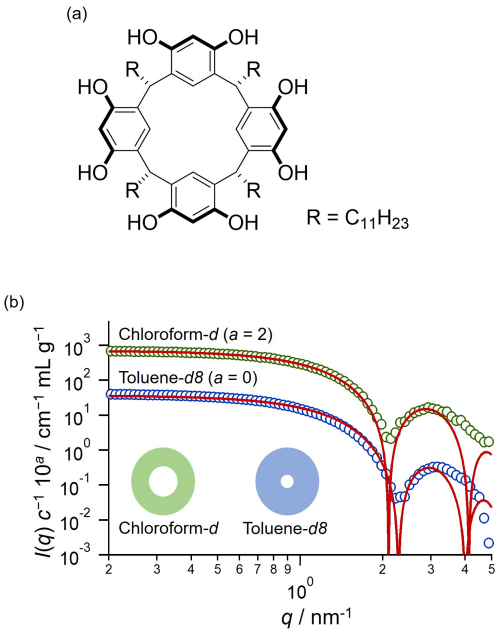

Fig. 1. Figure 1. (a) Chemical structure of C-undecylresorcinarene. (b) SANS profiles of C-undecylresorcinarene capsule. The red curves were calculated using spherical hollow model whose cross-sectional images are inserted.

Elucidating hydration state of poly (propylene oxide) in the glyco polymer vesicle membranes by SANS measurement.

Tomoki Nishimura
Kyoto University, Graduate school of engineering, Department of polymer chemistry

We have recently developed intrinsically permeable polymer vesicles based on maltopentaose-b-poly(propylene oxide) block-co-polymers (Figure 1a).[1] In aqueous solution, the polymer self-assembles into unilamellar vesicles. In contrast to other vesicles, the vesicles show molecular-weight-dependent molecular permeability. Low-molecular-weight compounds ($< 5 \times$ 10^3 g/mol) diffuse into the vesicles. We also proved that the permeability is due to the partition of solute molecules into the polymer membrane. Accordingly, we hypothesized that this permeation should be ascribed to the weakly hydrophilic nature of the PPO block. Specifically, the degree of hydration of the PPO layer in the membrane should contribute to facilitating the partition and, therefore, enhance molecular permeation.

To determine the degree of hydration of the PPO layer in the membrane, we previously used SAXS measurements in a preliminary study to obtain the corresponding electron-density profile using a theoretical fitting equation from a bilayer membrane model. The model fit of the SAXS data was consistent with an electron density of the hydrophobic layer (330 e/nm^3) that is almost identical to that of solvent (H2O; 334 e/nm^3). Given that the electron density of PPO is comparable to that of H2O, the degree of hydration in the PPO layer cannot be quantified using SAXS measurements.

We therefore proposed to subject carbohydrate-b-PPO vesicles to SANS measurements in order to quantify the degree of hydration of the PPO layer in the polymer-bilayer membranes of such polymer vesicles. Figure 1b shows SANS profile from maltopentaose-b-poly(propylene oxide) block polymer vesicles in D2O. The scattering curve showed a slope of -2 at low q region, suggesting the presence of thin plate structure. To gain further structural information, the scattering curve was fitted with the bilayer membrane model, which provide information on a bilayer cross-sectional structure. The model fits the SAXS data almost overall q-range and is consistent with a hydrophobic layer thickness of 9.3 nm, hydrophilic layer thickness of 2.0 nm, SLD of a hydrophobic layer (PPO layer) of 1.0 $\times$ 10^10 cm^-2 and SLD of a hydrophilic layer (maltopentaose layer) of 6.4 $\times$ 10^10 cm^-2 (Figure 1c). The size of hydrophobic and hydrophilic segment was identical to the data obtained from the previous SAXS analysis. It should be noted that SLD of the PPO layer was much higher than theoretical SLD value of PPO (3.43 $\times$ 10^9 cm^-2). This difference can be attributed to the hydration of PPO with D2O. To obtain volume fraction of D2O in PPO layers, we assumed that all the entire polymers are included in the bilayer region of the vesicles. We also imposed the hydrophobic layer is composed of all the PPO group and of a small amount of D2O. Based on these assumptions, we are able to calculate the volume fraction of D2O in the PPO layer by using following equation.

ρ _core=y_core ρ _ppo+(1-y_core) ρ _D2O

, where ρ _core, ρ _ppo, ρ _D2O, ycore is experimental SLD value of PPO layer, theoretical SLD value of PPO, theoretical SLD value of D2O, and volume fraction of PPO in the hydrophobic layer, respectively. The volume fraction of D2O in PPO layer was calculated to be ca. 11% by above equation. More interestingly, in the presence of kosmotropic salt such as Na2SO4, the SLD of hydrophobic layer was decreased to 5.5 $\times$ 10^10 cm^-2, indicating that the degree of hydration in the hydrophobic layer reduced. Since the degree of hydra-

tion would affect on the molecular permeability as mentioned above, the rate of molecular permeation would be controlled by changing external environment.

In summary, we conducted SANS measurements of maltopentaose-block-poly(propylene oxide) in D2O. We successfully obtained a clear evidence for the hydration of the hydrophobic PPO layer in the polymer bilayer membrane and were able to quantify the volume fraction of D2O in PPO layer. To the best of our knowledge, this is the first observation showing the hydration of hydrophobic layer in polymer bilayer membranes.

[1] T. Nishimura, Y. Sasaki, K. Akiyoshi, Adv. Mater., 2017, 29, 1702406

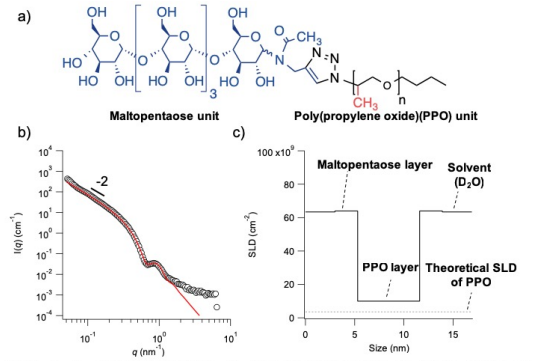

Figure 1 a) Chemical structure of maltopentaose-b-PPO, b) SANS profile of maltopentaose-b-PPO vesicles and a theoretical curve from the bilayer membrane model, c) SLD profile of maltopentaose-b-PPO vesicles

Fig. 1. a) Chemical structure of maltopentaose-b-PPO, b) SANS profile of maltopentaose-b-PPO vesicles and a theoretical curve from the bilayer membrane model, c) SLD profile of maltopentaose-b-PPO vesicles

Distribution of Additives in Ordered-Bicontinuos-Double-Network Structure Formed in Block Copolymer Systems Revealed by Small Angle Neutron Scattering

Katsuhiro Yamamoto(A), Tsukasa Miyazaki(B), Isamu Akiba(C)
(A)Nagoya Institute of Technology, (B)CROSS, (C)The University of Kitakyushu

Introduction. It is well known that block copolymer forms several periodic network structures due to phase-separation with nanoscale features. Well-defined network nanostructures have been expected to be utilized as hybrid porous filtration membranes, photonic crystals, and optical metamaterials, etc. There are two types of defined bicontinuous network structure in a block copolymer: gyroid (Gyr) and Fddd. Gyr is constructed from 3-fold nodes connected with Ia3d symmetry, whereas Fddd also has 3-fold nodes but has an orthorhombic unit cell. Recently, an ordered-bicontinuous- double-diamond (OBDD) structure which is constructed by 4-fold nodes connected with Pn3m symmetry was discovered in syndiotactic polypropylene(sPP)-polystyrene(PS) block copolymer [1,2]. The reason why the OBDD in this copolymer was thermodynamically stabilized was that the higher packing frustration of block copolymer chains in nodes was relaxed due to the existence of the population of helical segments of sPP. We also discovered OBDD structure in PS-b-polyisoprene(PI) (PS-b-PI) blended with PI. OBDD structures in Block copolymer (BCP)/HP systems was theoretically predicted [3,4] and experimentally observed [5]. Pure BCP melt never forms OBDD except for those with a favored helical conformation of sPP as mentioned above. However, in a BCP/HP system, the addition of the HP may reduce the frustration due to localization of the HP in the nodes, which is likely to occur when HP is longer than the identical chain in a BCP. The localization of the HP at the specific site is the key to understand the stabilization of OBDD. We aim to elucidate this point experimentally. SAXS experiment for such a system gives only morphological information, i.e., emergence of the OBDD. On the other hand, SANS expectedly gives not only morphology but also information of the distribution of the HP added when deuterated HP is used. We expect that the SANS profile will be very different from SAXS one if the added deuterated HP is located in specific sites.

Experimental. PS-b-PI (Mn,PS = 32800, Mn,PI = 18500, Mw/Mn = 1.03, volume fraction of PS = 38.6 vol%, NMR) synthesized by anionic polymerization. Fully deuterated PI (dPI) (Mn = 20,000) was purchased from Polymer Source Incorporation. Block copolymer PS-b-PI and homopolymer dPI were mixed in toluene and blended film samples were made from slow casting at 25 degree C for a week. Dried film samples were further dried at 140 degree C in a vacuum oven for 72 h. The films were cut into diameter of 1.5 cm and thickness of 0.5 mm. Blend ratios of dPI relative to PS-b-PI was 15, 20, and 25 wt%. Chain length ratio of BCP to dPI and the blend ratio was chosen to be form ordered double diamond network structure, which was predicted in literature [3,4] and our previous work [5]. SAXS and SANS measurements were conducted at BL10C (wave length of X-ray 0.1nm, camera length 3 m) in Photon Factory KEK (Tsukuba) and at BILBY (time-of-flight) in ANSTO (Australia), respectively.

Result and Discussion. Figure 1 shows SAXS and SANS profiles of PS-b-PI/dPI with a blend ratio of 25wt%. SAXS profile of the original PS-b-PI was also indicated in Figure 1. Original PS-b-PI indicates a hexagonally packed cylindrical morphology. As dPI was blended in PS-b-PI, the morphology changed to others depending

on the blend ratio of dPI. When the blend ratios of 15 and 20 wt%, the microphase separated structure was Gyr. At higher the blend ratio, the morphology was the cylinders with a larger lattice constant. (the periodicity became large). SANS profiles also indicated the identical structures observed in SAXS. In the case of blend ratio of 15 and 20 wt%, the difference in scattering profile between SAXS and SANS was small, indicating dPI was distributed uniformly PI domain. On the other hand, the significant difference was clearly observed at blend ratio of 25 wt%, e.g., the intensity of the first order peak in SANS was relatively smaller than that in the SAXS. This difference can be interpreted by taking into account for homopolymer distribution in the PI domain. Chain length of dPI was larger than that in BCP, meaning the "dry-brush" system. The dPI can be distributed preferentially in the core-region of the PI domain. SAXS and SANS profile were fitted with calculation (paracrystal distortion theory) of cylindrical model as shown in Figure 1 for the PS-b-PI/dPI (25wt%) sample. As for pure BCP, the estimated volume fraction of cylindrical domain was 33.3 vol% that is slightly deviated from the value estimated from NMR because of a larger error in NMR. In the blend system, the radius of the cylinder obtained in SANS fitting was found to be smaller than that in SAXS. Based on the volume fraction (40 vol%) of cylinder obtained from SAXS after blending, added dPI was mostly dissolved in PI domains. In the SANS measurement, the scattering contrast between deuterated region and hydrogenated materials is enhanced. Thus dPI distributed region was shown up. Thinner cylinder indicates the dPI should distribute in the core of the PI cylinder. From the value of the volume fraction of thin cylinder, most of the dPI was located in the core-region. Unfortunately, we did not get morphology of OBDD. This may be caused by inappropriate chain length ratio of dPI to BCP for forming the OBDD.

References
[1]C.-Y. Chu, et al., Macromolecules 45, (2012) 2471.
[2]C.-Y. Chu, et al. Soft matter 11, (2015) 1871.
[3]M.W.Matsen, Macromolecules 28 (1995) 5765.
[4]M.-V.Francisco J. et al. Macromolecules 42 (2009) 9058.
[5]H.Takagi, et al. EPL 110 (2015), 48003.

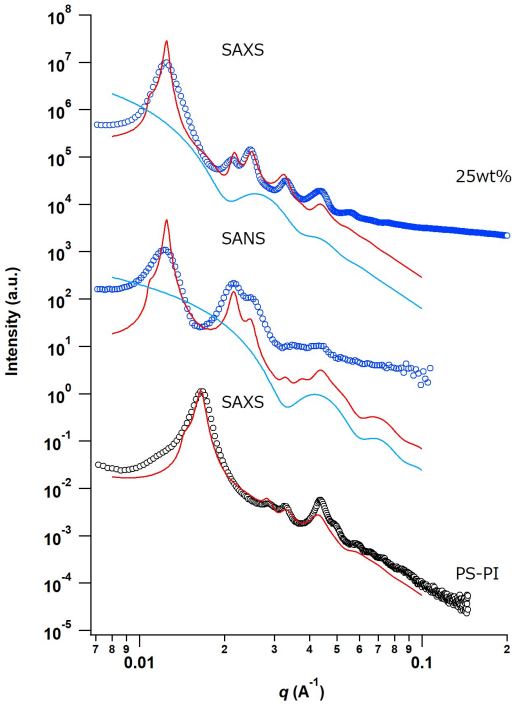

Fig. 1. SAXS (symbols) and SANS (lines) profiles of PS-b-PI/dPI with dPI blend ratio of 25wt% and PS-b-PI. The solid lines were obtained from the calculation. Blue lines indicate the form factor of the cylinder.

Investigation of Microscopic Structural Changes in Poly(oligo-ethylene glycol methyl ether methacrylate)-Based Hydrogels

Takuma Kureha, Xiang Li
The Institute for Solid State Physics

Polymer hydrogels are soft and water-swollen materials. Physicochemical properties, such as polarity and softness of gels, can be changed greatly by the stimuli-responsiveness of hydrogels, which make hydrogels promising materials for the advanced applications, including controlled uptake/release and actuators. More recently, poly(oligo-ethylene glycol methyl ether methacrylate) (POEGMA)-based polymers have been developed as a new type of thermo-responsive polymer (Lutz et al., Macromolecules 2006, 39, 893-896.). They offer a potential alternative to the use of thermo-responsive polymers and PEG for a design of hydrogels for biomedical applications.

However, to the best of our knowledge, very few studies have been reported on the physical properties of POEGMA-based gels, especially for the volume transition during changes in temperature. So far, we have investigated the dynamics of POEGMA-based gels by dynamic light scattering (DLS) (Kureha et al., Macromolecules 2018, 51, 8932-8939). Here, the formation mechanism of hydrophobic domains in the gels was investigated from the slow mode in the correlation functions. The hydrophobic domains composed of polymer aggregation grew in the gels by rising temperature and they were copolymerization ratio dependent. The domain formation was suppressed as the copolymerization ratio of the longer side chain was increased.

In this study, in order to investigate the domain formation mechanism in the molecular level, we carried out a systematic study of network structural changes in POEGMA gels by small-angle neutron scattering (SANS) as a function of temperature.

SANS results of POEGMA gels show the peak (Fig. 1), which correspond to the characteristic distance between the hydrophobic domains. Moreover, with increasing temperature, the scattering contribution of the peak was gradually decreased, suggesting that the correlation of the distance between domains disappeared because the heterogeneity of the polymer network was increased due to the growth of domain.

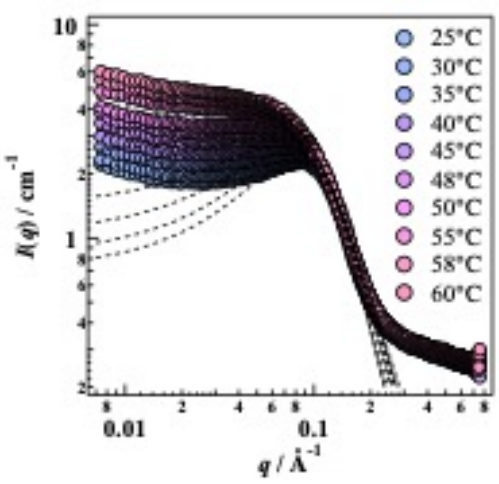

Fig. 1. Temperature dependence of SANS profiles of POEGMA-based gels.

Structural Characterization of DNA-module gel by Small-Angle Neutron Scattering

Masashi Ohira, Xiang Li, and Mitsuhiro Shibayama
The Institute for Solid State Physics, The University of Tokyo

Physical gels such as gelatin gel or agarose gel, which exist generally like natural materials, are used in various fields, such as food, industrial and medical applications. They are composed of polymer networks crosslinked with physical bonding such as hydrogen bonding, Coulomb ' s interaction or hydrophobic interactions. In conventional chemical or physical gels, it is restricted to control the polymer network of physical gels due to the randomness of crosslinking (branching) and the network structure became very heterogeneous. However, by a simple strategy, just mixing two mutual four-arm polyethylene glycols carrying reactive end-groups together, the network will be homogenized because the branching point in each tetra-PEG macromer is uniformly distributed in the network (Figure 1). Our previous SANS study has proved the excellent homogeneity of networks of tetra-PEG gels.

Recently, we have applied the strategy of tetra-PEG gel into physical gels by modifying the chemically reactive end-group on each arm of tetra-PEG to a physically reactive end-group: sense and anti-sense single-stranded DNA (Figure 1). Because of the high specificity of hydrogen binding between two complementary DNA, the reproducible sol-gel transition was observed by rheological measurement. We carried out small angle neutron scattering with Quokka at ANSTO to investigate its thermo-dependency of the structure. In the previous study, the data is a bit complicated because it contains both PEG and DNA information. In this proposed experiment, in order to focus PEG polymer and DNA crosslinkers exclusively and obtain more accurate information about PEG and DNA structural change such as association and dissociation of double-helix along with the sol-gel transition. Thus, we investigated this gel with SANS measurement with a contrast matching technique.

The SANS measurement result is shown in Figure 2. With elevating temperature, scattering intensity becomes bigger but SANS profiles do not change clearly at the sol-gel transition point (Tgel ~ 60 ℃) and the melting point of double-stranded DNA. Therefore, this gel has a homogenous structure. Additionally, the SANS profile does not have hysteresis.

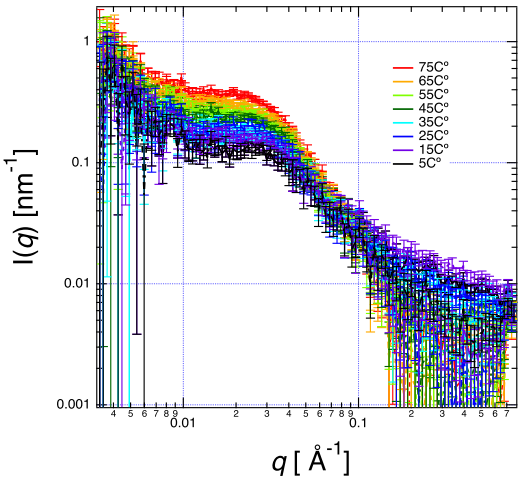

Fig. 1. The SANS profiles of DNA-module gel at various temperature

Length dependent effect of added alkane on fluidity and inter-leaflet coupling of lipid membranes

Hatsuho Usuda[1], Mafumi Hishida[1], Elizabeth Kelley[2], Michihiro Nagao[3]
[1]*Dept. Chem. Univ. Tsukuba,* [2]*NIST Center for Neutron Research,* [3]*Dept. Phys. Indiana Univ.*

[Background] In biomembranes, various kinds of small organic molecules, such as sterols and fatty acids, regulate the physical properties of lipid bilayers to maintain cell functions. One of the typical effects of these organic molecules is on membrane fluidity, which has long been an important topic in biomembranes. Studies in biologically relevant systems have suggested that membrane fluidity affects various cell functions, such as enzyme activity, transport process, hormone action, and immune response. [1] Not only the bilayer's fluidity itself but also the dynamic coupling/decoupling of the outer and inner leaflets of bilayers is possibly controlled by such small organic molecules. However, the effects of small organic molecules on the bilayer fluidity and the inter-leaflet coupling have not been fully understood.

The inter-leaflet coupling is known to connect the elastic bending modulus, κ, and the area compressibility modulus, K_A, in a thin elastic sheet theory. [2] As explained more in detail in the following section, recent neutron spin echo (NSE) studies start to measure both κ and K_A independently by measuring both bending and thickness fluctuations in a lipid bilayer. [3,4]

In this experiment, we investigated the effect of small organic molecules on the membrane fluidity utilizing NSE. We used synthetic lipid bilayers with *n*-alkanes. The effects of *n*-alkanes on the phase behavior, the bilayer structure, and its elasticity, have been extensively studied by us. [5,6] Change in the phase behavior of the lipid bilayers strongly depends on the alkane length.[5] We speculated that the membrane fluidity also relates to the intermolecular force in the membrane. For the systematic understanding of the effects of various organic molecules on the membrane properties, the alkane length dependence of the membrane fluidity will be an ideal system to explore.

[Methods] The NSE technique has been traditionally used to determine membrane's elastic bending modulus, κ. However, the recent development of membrane theories and experimental techniques started to shed light on more detailed membrane properties. [7,8]

Recently, thickness fluctuations in lipid membranes have been successfully measured using NSE, [3,4,9] and this technique was shown to be potential means to access β, which characterizes the inter-leaflet coupling. [4] The bending fluctuations have been modeled by Zilman and Granek [10] as the intermediate scattering function decays following a stretched exponential function with a stretching exponent of 2/3. The decay rate $\Gamma(q)$, where q is the momentum transfer, follows q^3 for bending fluctuations, while the thickness fluctuations are seen as a peak in $\Gamma(q)/q^3$ with an underlying q^3 dependence as follows: [4]

$$\frac{\Gamma}{q^3} = 0.0069\sqrt{\frac{k_B T}{\kappa}}\frac{k_B T}{\eta} + \frac{(\tau_{TF} q_0^3)^{-1}}{1+(q-q_0)^2\xi^2} \quad (1)$$

where the first term indicates the contribution from the bending fluctuations and the second term represents the thickness fluctuation contributions. η is the solvent viscosity, τ_{TF} represents the relaxation time for the thickness fluctuations, q_0 denotes the peak location in Γ/q^3 representation which is identical to the dip location of the bilayer form factor measured by SANS, and ξ indicates the half width at half maximum (HWHM) of the Lorentz function. The fractional change in the thickness, σ_h, is ex-

pressed as $\sigma_h = \Delta h/h = 2(q_0\xi)^{-1}$, where h represents the bilayer thickness. Neglecting changes of the molecular volume, σ_h is compensated for by the fractional change in the area, σ_A, as $\sigma_h^2 = \sigma_A^2$, and a simple statistical mechanical relation connects area compressibility modulus K_A and σ_h as $K_A = k_B T/\sigma_h^2 A_0$. [4,11] Therefore, the measurement of the thickness fluctuation amplitude yields to estimate K_A. On the other hand, in a thin elastic sheet theory, a relation between κ and K_A is formulated as $K_A = \beta\kappa/d_t^2$, where d_t is the thickness of the hydrocarbon region of the membrane. [2] These two independent measure of κ and K_A by the bending and thickness fluctuations, respectively, allows one to estimate a change in β if any.

[Results] We have performed an NSE experiment on the NGA-NSE and SANS experiment on the NG7, NIST, using dipalmytoylphosphatidylcholine (DPPC) bilayers with and without alkanes. We measured the cases for *n*-octane (C8), *n*-decane (C10), *n*-dodecane (C12) and *n*-tetradecane (C14). We independently measured the bending and thickness fluctuations by using protiated and alkanes in D_2O for the bending fluctuations, while the thickness fluctuation measurements were performed by employing tail-deuterated DPPC, deuterated *n*-alkanes and D_2O.

As the alkane length increased, κ became lower, which means that the membrane became more flexible. This trend is very interesting considering SANS results indicating that membrane thickness increases with increasing the alkane length. The thickness change is also supported by the results of thickness fluctuations (Fig. **??**). The peak derived from thickness fluctuation shifted to lower-q with increasing alkane length. κ should be larger as membrane thickness becomes larger if the membrane viscosity and molecular volume are not changed by the incorporation. Therefore, the decrease in κ suggests the possibility of changes in them. As peak width ξ is inversely proportional to thickness fluctuation amplitude ($\sigma_h = 2(q_0\xi)^{-1}$), the observed increase in ξ indicates that the thickness fluctuation is suppressed by *n*-alkanes. The results also show the alkane length dependence of ξ. It is possible that shorter alkane changes the membrane structure or viscosity more largely, resulting in the larger suppress.

[1] J. Szöllösi, in *Mobility and proximity in biological membranes*, CRC Press (1994). Haracska, G. Bogdanovics, Z. Torok, I. Horvath, L. Vigh, *Int. J. Hyperthermia* **29**, 491 (2013).

[2] D. Boal, in *Mechanics of the Cell*, 2nd Ed.; Cambridge University Press, 267 (2002).

[3] A.C. Woodka, P.D. Butler, L. Porcar, B. Farago, M. Nagao, *Phys. Rev. Lett.* **109**, 058102 (2012).

[4] M. Nagao, E.G. Kelley, R. Ashkar, R. Bradbury, P.D. Butler, *J. Phys. Chem. Lett.* **8**, 4679 (2017).

[5] M. Hishida, A. Endo, K. Nakazawa, Y. Yamamura, K. Saito, *Chem. Phys. Lipids*, **188**, 61 (2015).

[6] M. Hishida, R. Yanagisawa, H. Usuda, Y. Yamamura, K. Saito, *J. Chem. Phys.* **144**, 041103 (2016).

[7] M.C. Watson, E.S. Penev, P.M. Welch, F.L.H. Brown, *J. Chem. Phys.* **135**, 244701 (2011).

[8] J.F. Nagle, *Phys. Rev. E* **96**, 030401(R) (2017).

[9] M. Nagao, *Phys. Rev. E* **80**, 031606 (2009).

[10] A.G. Zilman, R. Granek, *Phys. Rev. Lett.* **77**, 4788 (1996).

[11] M.P. Allen, D.J. Tildesley, *Computer Simulation of Liquids*, Clarendon Press, Oxford, 43-54 (1987).

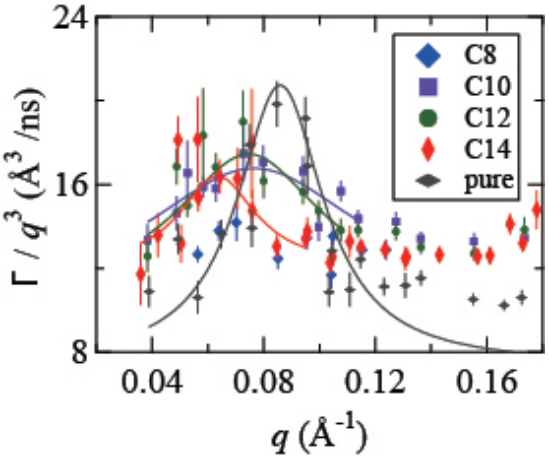

Fig. 1. $\Gamma(q)/q^3$ for DPPC with and without alkanes (C8 C10, C12 and C14). Red diamond: our unpublished previous result. Black diamond: result from [4].

Investigation of Microscopic Structural Changes in Poly(oligo-ethylene glycol methyl ether methacrylate)-Based Hydrogels

Takuma Kureha, Xiang Li
The Institute for Solid State Physics

Polymer hydrogels are soft and water-swollen materials. Physicochemical properties, such as polarity and softness of gels, can be changed greatly by the stimuli-responsiveness of hydrogels, which make hydrogels promising materials for the advanced applications, including controlled uptake/release and actuators. More recently, poly(oligo-ethylene glycol methyl ether methacrylate) (POEGMA)-based polymers have been developed as a new type of thermo-responsive polymer (Lutz et al., Macromolecules 2006, 39, 893-896.). They offer a potential alternative to the use of thermo-responsive polymers and PEG for a design of hydrogels for biomedical applications.

However, to the best of our knowledge, very few studies have been reported on the physical properties of POEGMA-based gels, especially for the volume transition during changes in temperature. So far, we have investigated the dynamics of POEGMA-based gels by dynamic light scattering (DLS) (Kureha et al., Macromolecules 2018, 51, 8932-8939). Here, the formation mechanism of hydrophobic domains in the gels was investigated from the slow mode in the correlation functions. The hydrophobic domains composed of polymer aggregation grew in the gels by rising temperature and they were copolymerization ratio dependent. The domain formation was suppressed as the copolymerization ratio of the longer side chain was increased.

In this study, in order to investigate the domain formation mechanism in the molecular level, we carried out a systematic study of network structural changes in POEGMA gels by small-angle neutron scattering (SANS) as a function of temperature.

SANS results of POEGMA gels show the peak (Fig. 1), which correspond to the characteristic distance between the hydrophobic domains. Moreover, with increasing temperature, the scattering contribution of the peak was gradually decreased, suggesting that the correlation of the distance between domains disappeared because the heterogeneity of the polymer network was increased due to the growth of domain.

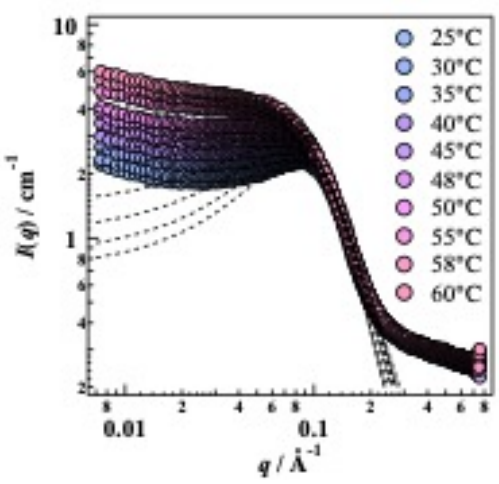

Fig. 1. Fig.1. Temperature dependence of SANS profiles of POEGMA-based gels.